NASA Contractor Report 3906

A Three-Dimensional Viscous Flow Analysis for the Helicopter Tip Vortex Generation Problem

S.-J. Lin, R. Levy,
S. J. Shamroth, and T. R. Govindan

CONTRACT NAS1-14904
AUGUST 1985

NASA

NASA Contractor Report 3906

A Three-Dimensional Viscous Flow Analysis for the Helicopter Tip Vortex Generation Problem

S.-J. Lin, R. Levy,
S. J. Shamroth, and T. R. Govindan
Scientific Research Associates, Inc.
Glastonbury, Connecticut

Prepared for
Langley Research Center
under Contract NAS1-14904

National Aeronautics
and Space Administration

**Scientific and Technical
Information Branch**

1985

TABLE OF CONTENTS

INTRODUCTION

An important and difficult problem of rotor aerodynamics is the three-dimensional viscous flow field occurring in the vicinity of the rotor tip. The tip region contains a complex three-dimensional viscous flow field which results from the unequal pressures on the upper and lower surfaces on a lifting airfoil. Since at the rotor tip a pressure discontinuity is not possible, the pressure difference across the blade is gradually relieved towards the tip until the pressures on both sides are equal at the tip. Associated with this pressure field is a secondary flow field outward on the pressure surface, around the tip, and inward on the suction surface. This secondary flow convects low momentum fluid from the pressure side around the tip to the suction side. The low momentum fluid accumulates on the suction side of the tip, rolls up and forms the tip vortex which then is convected downstream by the streamwise velocity.

The details of the flow in the tip region can have a major effect in determining the generated rotor noise and can significantly affect the performance and dynamic loading of the rotor blade. In addition, the tip vortex generated by a given blade may interact with the following blade significantly modifying the oncoming flow encountered by the following blade, thus affecting the following blade's performance. Although the motivation of the present study is the helicoptor rotor tip vortex problem, this is not the only important physical flow situation in which the tip vortex plays a prominent role. The tip vortex also plays a prominent role in flow about wing tips of large aircraft which can affect cruise efficiency and can cause hazardous conditions for following aircraft encountering the tip vortex wake. The leading edge vortex plays a major role in determining the performance of delta wings. Other applications for tip vortex analysis occur in hydrodynamic flow situations. Typical examples can be found associated with ship or submarine propellers and the submarine sail.

To date, most efforts which have focused upon the tip flow field problem have been either experimental investigations primarily confined to regions downstream of the blade, or analytic efforts primarily confined to inviscid analyses. For example Scheiman, Megrail and Shivers (Ref. 1)

utilized a tuft grid technique to investigate the vortex downstream of a fixed airfoil. Although their investigation showed the problem to have a definite Reynolds number effect on core size, they were not able to define a functional relationship between core size and lift, drag or induced drag. Thompson (Ref. 2) used a tow tank and hydrogen bubble technique to study axial flow in wing tip vortices downstream of the airfoil trailing edge. Spivey and Morehouse (Ref. 3) compared the performance of swept tip and square tip shapes in both wind tunnels and whirl stand environments through flow visualization tests and surface pressure measurements in the blade tip region. Francis and Kennedy (Ref. 4) obtained hot wire measurements in the tip region, and Chigier and Corsiglia (Refs. 5 and 6) also using hot wire probes measured tip region velocities both upstream and downstream of the airfoil trailing edge. Finally, Geissler (Ref. 7) and Shivanada, McMahon and Gray (Ref. 8) measured tip pressure distributions. In regard to ship propeller studies a survey of literature has been made by Platzer and Souders (Ref. 9), and experiments have been carried out by Souders and Platzer (Ref. 18) as well as Jessup (Ref. 11). Although not directly related to the helicopter rotor blade problem, numerous other studies have focused upon far field wake-vortex characteristics (e.g., Ref. 12). As may be discerned from the previous discussion, most experimental efforts in this area have concentrated upon the flow downstream of the airfoil trailing edge. Some surface pressure data has been taken on the airfoil itself (e.g., Refs. 3, 5, and 8), and some flow field data has been taken upstream of the airfoil trailing edge (Refs. 4-6). However, the flow region usually investigated is in that region aft of the airfoil.

A review of the analytic approaches to this problem shows that for the most part these are based upon inviscid formulations. For example, Kandil, Mook and Nayfeh (Refs. 13 and 14) and Rehbach (Ref. 15) have applied vortex lattice methods to predict vortex roll-up in the region over both rectangular and delta wings. Similar lifting surface-type analysis have been presented by Maskew (Ref. 16) for the helicopter applications and by Kerwin and Lee (Ref. 17), Greeley and Kerwin (Ref. 18) and Brockett (Ref. 19) for ship propeller applications.

Although vortex lattice methods are useful in predicting overall flow properties such as lift coefficients, the methods contain some inherent

properties which preclude their applicability to the more detailed aspects of the tip vortex problem. Since they are inviscid, the vortex lattice methods do not model the physical mechanisms of viscous generation of vorticity at no-slip flow boundaries and the subsequent combined convection, diffusion and dissipation of wall generated vorticity. Also variations in details of tip shape which may effect vortex generation are difficult to represent properly in a vortex-lattice analysis.

The limitations which are inherent in vortex lattice or other inviscid methods have motivated the development of alternate calculation procedures for the tip vortex problem. One such possible procedure would be a solution of the full Navier-Stokes equations. Upon hypothesis of a suitable turbulence model, the Navier-Stokes equations contain all the required mechanisms present in the tip vortex flow field and the compressible Navier-Stokes equations have been used to predict complex two- and three-dimensional flows (e.g., Refs. 20 and 21). However, solution of the three-dimensional viscous flow problem in the airfoil tip region via the Navier-Stokes equations would require a large number of grid points to resolve the required physical scales. This would lead to computer run times which at present are not practical on a routine basis. Hence, an alternative and more economical three-dimensional viscous flow approach was adopted for the present investigation.

Over the past few years, several investigators have suggested methods aimed at obtaining a physically realistic and numerically sound forward marching procedure for three-dimensional viscous flows. In general, these methods utilize an extended boundary layer approach based on approximate governing equations which suppress streamwise elliptic effects requiring downstream boundary conditions. Motivated by these same goals, Briley and McDonald (Ref 22) have developed a new viscous primary/secondary flow analysis for the prediction of a wide class of subsonic flows at high Reynolds number in straight or smoothly curved flow geometries.

More recently this approach has been refined and modified to remove some of the assumptions previously required to obtain a viable forward marching procedure (Ref. 23). The approach is applicable to flows which have a predominant primary flow direction with transverse secondary flow, and synthesizes concepts from inviscid flow theory, secondary flow theory, and "extended" three-dimensional boundary layer theory. The analysis

utilizes a set of viscous flow equations and imposes no-slip boundary conditions on solid boundaries. The analysis also does not require small cross-flows and in fact allows cross flows of the magnitude of the primary flow. The analysis is expected to obtain a flow field calculation in a run time at least an order of magnitude faster than a Navier-Stokes solution using the same number of grid points, thus presenting a significant run time advantage. As will be shown subsequently in the case of the tip vortex, the analysis calculates the vortex formation from cross flow separation of the boundary layer as it is carried around the blade tip. As discussed in Ref. 4, this is clearly the physical mechanism of tip vortex formation and, therefore, the basic physics of the flow are modelled in the equations. In Refs. 22 and 23, Briley and McDonald applied this analysis to three-dimensional flow in curved passages and predicted the development of the passage flow field including the formation and development of passage and corner vortices. This same approach has been applied at SRA to the problems of flow in circular ducts with curved centerlines (Ref. 24), lobe mixer flows (Ref. 25), and further passage studies (Ref. 26). Under the present contract this approach has been further developed with a view toward the tip vortex problem. Interim reports on this effort are given in Ref. 27,and an application to the ship propeller problem is demonstrated in Ref. 28.

The present report details the effort under the subject contract. It contains both material from Ref. 27 and new results obtained since that report. The following sections discuss analysis, numerical methods, boundary conditions, etc. and gives results for a variety of laminar and turbulent test cases.

LIST OF SYMBOLS

U_p	primary velocity
Ω_n	secondary vorticity
U_s	secondary velocity
ϕ	scalar surface potential
ψ	vector surface potential
ρ	density
ρ_o	reference density
U	total velocity
P	static pressure
R	gas constant
T	temperature
T_o	stagnation temperature
C_p	heat capacity
x	streamwise direction
y	vertical direction
z	spanwise direction
C	length of chord
u_e	free stream velocity
μ	laminar viscosity
ϵ	turbulent viscosity
δ	boundary layer thickness
Re	Reynolds number = $\rho u_e C/\mu$
M	Mach number = u_e/a
a	sound velocity

ANALYSIS

General

The analysis of three-dimensional viscous flow fields such as that in the airfoil tip region presents a very difficult task for the computational fluid dynamicist. One possible mode of attack would solve the full three-dimensional Navier-Stokes equations. Although successful calculations of the compressible three-dimensional Navier-Stokes equations have been made for complex flow situations (e.g., Ref. 21), these solutions of necessity require both relatively large computer storage and relatively long run times. Although they have reached the point where they can be used to analyze flow fields, they are most attractive when no suitable alternative exists. In the airfoil tip flow field problem a three-dimensional Navier-Stokes analysis would require a large enough number of grid points to determine the pressure distribution as well as to calculate and suitably resolve the thin viscous flow regions in the immediate vicinity of the airfoil surface. With present computers the number of grid points required for such a task would require large quantities of computer run time. Thus, an alternative and more economical calculation procedure is desired.

One promising method would be a three-dimensional viscous flow foward-marching analysis. Such techniques have been developed for steady flows which satisfy two requirements; (i) they must have an approximate primary flow direction which can be specified a priori and (ii) flow derivatives in this approximate primary direction must be considerably smaller than flow derivatives normal to this direction. Obviously, the tip flow field satisfies these requirements aft of the leading edge and, therefore, is a candidate for a three-dimensional viscous forward marching approach. The approach used in the present effort is based upon the work of Briley and McDonald (Ref. 22). This procedure has proven very successful in the calculation of three-dimensional viscous internal flows containing strong streamwise vorticity. Calculations giving detailed comparison with experimental data for a variety of passage flows are given by Levy, Briley and McDonald in Ref. 24. The present section details this analysis with particular attention paid to the tip vortex generation process.

The governing equations which are used in the analysis are derived from the time averaged Navier-Stokes equation through approximations made relative to a curvilinear coordinate system fitted to and aligned with the flow geometry under consideration. The coordinate system is chosen such that the streamwise or marching coordinate either coincides with or is at least approximately aligned with a known inviscid primary flow direction as determined, for example, by a potential flow for the given geometry. Transverse coordinate surfaces must be approximately perpendicular to solid walls or bounding surfaces, since diffusion is permitted only in these transverse coordinate surfaces.

Equations governing primary flow velocity U_p, and a secondary vorticity, Ω_n, normal to transverse coordinate surfaces are derived utilizing approximations which permit solution of the equations as an initial-value problem, provided reversal of the composite streamwise velocity does not occur. Calculations can be continued through regions of limited separation by neglecting streamwise convective terms in the reversed flow region. Terms representing diffusion normal to transverse coordinate surfaces (in the streamwise direction) are neglected. Secondary flow velocities are determined from scalar and vector surface potential calculations in transverse coordinate surfaces, once the primary velocity and secondary vorticity are known.

Primary-Secondary Velocity Decomposition

In the discussion which follows, vectors are denoted by an overbar, and unit vectors by a caret. The analysis is based on decomposition of the overall velocity vector field $\bar{U}$ into a primary flow velocity $\bar{U}_p$ and a

secondary flow velocity $\bar{U}_s$. The overall or composite velocity is determined from the superposition

$$\bar{U} = \bar{U}_p + \bar{U}_s \tag{1}$$

The primary flow velocity is represented as

$$\bar{U}_p = U_p \hat{i}_p \tag{2}$$

where $\hat{i}_p$ is a known inviscid primary flow direction determined for example from an a priori potential flow solution for the geometry under consideration. In many cases, a streamwise coordinate direction from a body fitted coordinate system is an adequate approximation to this potential flow direction. The primary velocity $\bar{U}_p$ is determined from solution of a primary flow momentum equation. The secondary flow velocity $\bar{U}_s$ is derived from scalar and vector surface potential denoted ϕ and ψ, respectively. If $\hat{i}_n$ denotes the unit vector normal to transverse coordinate surfaces, if ρ is density, and if ρ_o is an arbitrary constant reference density, then $\bar{U}_s$ is defined by

$$\bar{U}_s \equiv \nabla_s \phi + (\rho_o/\rho) \nabla \times \hat{i}_n \psi \tag{3}$$

where ∇_s is the surface gradient operator defined by

$$\nabla_s \equiv \nabla - \hat{i}_n (\hat{i}_n \cdot \nabla) \tag{4}$$

It follows that since $\hat{i}_n \cdot \bar{U}_s = 0$, then U_s lies entirely within transverse coordinate surfaces. Equation (3) is a general form permitting both rotational and irrotational secondary flows and will lead to governing equations which may be solved as an initial-boundary value problem. Based upon Eqs. (2) and (3), the overall velocity decomposition (1) can be written

$$\bar{U} = U_p \hat{i}_p + \nabla_s \phi + (\rho_o/\rho) \nabla \times \hat{i}_n \psi \tag{5}$$

Surface Potential Equations

Equations relating ϕ and ψ with U_p, ρ, and the secondary vorticity component Ω_n can be derived using Eq. (5) as follows: From continuity,

$$\nabla\cdot\rho\bar{U} = 0 = \nabla\cdot\rho U_p\hat{i}_p + \nabla\cdot\rho\nabla_s\phi + \rho_o\nabla\cdot\nabla x\hat{i}_n\psi \qquad (6)$$

and from the definition of the vorticity based on the secondary flow within the transverse surfaces, Ω_n

$$\hat{i}_n\cdot\nabla x\bar{U} \equiv \Omega_n = \hat{i}_n\cdot\nabla x\, U_p\hat{i}_p + \hat{i}_n\cdot\nabla x(\rho_o/\rho)\,\nabla x\,\hat{i}_n\psi + \hat{i}_n\cdot\nabla\, x\,\nabla_s\phi \qquad (7)$$

Since the last term in each of Eqs. (6 and 7) is zero by vector identity, Eqs. (6 and 7) can be written as

$$\nabla\cdot\rho\nabla_s\phi = -\nabla\cdot\rho U_p\hat{i}_p \qquad (8)$$

$$\hat{i}_n\cdot\nabla x\,(\rho_o/\rho)\,\nabla x\hat{i}_n\psi = \Omega_n - \hat{i}_n\cdot\nabla x\,U_p\hat{i}_p \qquad (9)$$

Note that the last term in Eq. (9) is identically zero in a coordinate system for which $\hat{i}_n$ and $\hat{i}_p$ have the same direction. Given a knowledge of U_p, Ω_n and ρ, the surface potentials ϕ and ψ can be determined by a two-dimensional elliptic calculation in transverse coordinate surfaces at each streamwise location. In turn, $\bar{U}_s$ can be computed from Eq. (3), and the composite velocity $\bar{U}$ will satisfy continuity. Equations for U_p and Ω_n are obtained from the equations governing momentum and vorticity, respectively.

The streamwise momentum equation is given by

$$\hat{i}_p\cdot[\,(\bar{U}\cdot\nabla)\bar{U} + (\nabla P)/\rho] = \hat{i}_p\cdot\bar{F} + \hat{i}_p\cdot\bar{R} \qquad (10)$$

where P is pressure, $\rho\bar{F}$ is force due to viscous stress and terms in $\bar{F}$ representing streamwise diffusion are neglected. $\rho\bar{R}$ is the additional force due to a rotating coordinate system; where $\bar{R} = -2\bar{\omega} \times \bar{U} - \bar{\omega}\times(\bar{\omega} \times \bar{r})$, ω is the angular velocity of the coordinate system and $\bar{r}$ is the radius vector from the rotation axis. For the present rotational effects have not been included in the cases considered although they have been included in the work of Ref. 28. The pressure term in the streamwise momentum equation (10) can be taken from a simpler analysis such as a potential flow analysis, and within the present analysis must be obtained from an external source. While this results in a set of equations which can be solved by forward marching, the surface pressures which are due to the pressure field imposed upon the flow are the potential flow pressures. Since the actual surface pressures are often of primary interest, a revised computation of the actual surface pressure which includes viscous and secondary flow effects can be obtained from the resulting velocity field in the following manner.

The momentum equations in the transverse surfaces are:

$$\begin{aligned} \hat{i}_1 \cdot [(\rho\bar{U} \cdot \nabla)\ \bar{U} + \nabla P - \rho\bar{F} - \rho\bar{R}] &= 0 \\ \hat{i}_2 \cdot [(\rho\bar{U} \cdot \nabla)\ \bar{U} + \nabla P - \rho\bar{F} - \rho\bar{R}] &= 0 \end{aligned} \tag{11}$$

Equation (11) represents components of the momentum vector in the transverse surfaces:

$$\begin{aligned} &\hat{i}_1\ (\hat{i}_1 \cdot [(\rho\bar{U} \cdot \nabla)\ \bar{U} + \nabla P - \rho\bar{F} - \rho\bar{R}]) \\ &+ \hat{i}_2\ (\hat{i}_2 \cdot [(\rho\bar{U} \cdot \nabla)\ \bar{U} + \nabla P - \rho\bar{F} - \rho\bar{R}]) \end{aligned} \tag{12}$$

The divergence of this vector can be written as a Poisson equation for the pressure P at each transverse surface:

$$\begin{aligned} \nabla_s^2 P = \nabla_s^2 (P_I + P_c) = &-\frac{\partial}{\partial x_1}\ (\hat{i}_1 \cdot [(\rho\bar{U} \cdot \nabla)\ \bar{U} - \rho\bar{F} - \rho\bar{R}]) \\ &- \frac{\partial}{\partial x_2}\ (\hat{i}_2 \cdot [(\rho\bar{U} \cdot \nabla)\ \bar{U} - \rho\bar{F} - \rho\bar{R}]) \end{aligned} \tag{13}$$

where P_I is the imposed pressure, obtained from an independent source such as an inviscid analysis, P_c is a viscous correction to the pressure field and x_1 and x_2 are coordinates in the $\hat{i}_1$ and $\hat{i}_2$ directions, respectively. Equation (13) can be solved for the pressure correction, P_c, at each computational station using Neuman boundary conditions derived from Eq. (12). The use of Neuman boundary conditions requires an additional parameter which is only a function of the normal direction, $P_v(x_3)$, in order to set the level of the pressure field. For internal flows $P_v(x_3)$ would be set to ensure that an integral mass flux condition is satisfied

$$\int_A \hat{i}_n \cdot \rho \bar{U} \, dA = \text{CONSTANT} \tag{14}$$

For external flows $P_v(x_3)$ is set to match the imposed pressure at an appropriate far field location. It should be noted that in a recent effort (Ref. 23) Briley and McDonald have modified this analysis so as to obtain the pressure field on the primary flow velocity as part of the solution procedure.

Secondary Vorticity

The equation governing Ω_n is obtained from the normal ($\hat{i}_n$) component of the curl of the vector momentum equation. The elimination of the pressure results in a single equation for the transport of the vorticity normal to the transverse surface. This equation has the form

$$\bar{U} \cdot \nabla \Omega_n - \bar{\Omega} \cdot \nabla U_n = G_n + C + \hat{i}_n \cdot (\nabla \times \bar{R}) \tag{15}$$

where G_n is the normal component of

$$\bar{G} = \nabla \times \dot{\bar{F}} \tag{16}$$

and C is a collection of curvature terms arising from changes in orientation of the transverse surfaces as a function of streamwise coordinate.

The Gas Law Equation

For incompressible flow density is a constant value and the Eqs. (8), (9), (10), (13) and (16) form the required governing set. For compressible flow an additional equation relating the density to the other flow variables is required. Such an equation is obtained fom the perfect gas law

$$p = \rho RT \tag{17}$$

Assuming constant total temperature, Eq. (17) can be written as

$$p = \rho R\left(T^{o} - \frac{\bar{U}\cdot\bar{U}}{2C_{p}}\right) \tag{18}$$

which relates density, pressure and velocity. If the total temperature assumption is inadequate an energy equation can be added to the system and solved coupled with the streamwise momentum equation.

Governing System of Equations

A complete system of five coupled equations governing U_p, Ω_n, ϕ and P is given by Eqs. (8), (9), (10), (13 and 15). Ancillary relations are given by Eq. (5) for composite velocity. In reference 29, these equations are given in general orthogonal coordinates and in reference 24 in nonorthogonal coordinates.

Boundary Conditions

Although boundary conditions have been discussed briefly in the previous subsections, it is advantageous to review and expand the discussion here. In regard to boundary conditions, three types of boundaries are present; these are the solid wall boundary at the airfoil, the free stream boundary and the inboard boundaries. Considering first the solid wall, this is a no-slip, no-through flow boundary. The primary velocity component is specified to be zero at the wall. The continuity equation is solved with $\partial\phi/\partial n = 0$ which

gives zero normal velocity and a non-zero wall slip velocity equal to V_t. Finally, the coupled stream function - vorticity set is solved subject to zero normal velocity and a tangential velocity specified as $-V_t$ thus giving a composite no-slip, no-through flow condition. At the freestream boundary the primary velocity is extrapolated from interior points. The scalar potential is set to a constant so that the tangential component of the irrotational velocity is zero. This condition allows outflow through the boundary due to the displacement effect of the boundary layer on the blade. The angle of attack of the flow specifies a component of the transverse velocity on the boundary. The vector potential is obtained by integrating this component of the transverse velocity along the boundary. The streamwise vorticity is set to zero. Finally, at inboard boundaries the spanwise derivative of the streamwise velocity is set to zero. The scalar potential is treated by setting its spanwise derivative to zero. The vector potential is set to a constant, and the streamwise vorticity set to zero. This corresponds to a two-dimensional flow situation at the inboard boundary.

A more recent treatment of this inboard boundary condition is now available where the two-dimensional assumption is replaced by computation of a velocity field indued by the entire rotor. This treatment permits the inboard boundary to be placed closer to the tip. Under this portion of the effort the inboard boundary conditions were reformulated to represent the influence of the inboard sections on the wing tip flow field. Thus, the specification of the inboard boundary conditions should be related to the velocity field of the wing which contains the influence of the lift distribution and the trailing vortex sheet of the entire wing. With these considerations in mind, a revised inboard boundary condition was formulated. In this approach a spanwise velocity distribution along the inboard boundaries compatible with the viscous flow equations is obtained from solution of the coupled vector potential-vorticity equations along the inboard boundaries utilizing the inviscid spanwise velocity as an outer boundary condition. Neglecting spanwise variations, the coupled vector potential-vorticity equations are solved as a two-point boundary value problem along the inboard boundaries. Boundary conditions are specified from the no-slip and no through-flow velocity conditions on the wing surface (at B - C of Fig. 22), and the inviscid spanwise velocity and zero streamwise vorticity at the outer boundary (at A - D of Fig. 22). The solution to

the vector potential is used as the inboard boundary condition for the coupled vector potential-vorticity equations for the interior tip flow field. When an inviscid velocity field about the wing is available, the spanwise velocity boundary condition is derived from this flow field as outlined. If an inviscid flow field is not available, the required inviscid flow information can be approximated from the induced velocity field derived from an assumed spanwise lift distribution.

Most of the calculations presented in this report were performed using the two-dimensionality assumption on the inboard boundary except those calculations presented at the end of the results section. The results of calculations performed using the revised boundary condition formulation are presented in the section entitled Inboard Boundary Condition Study.

Numerical Method

Since techniques for obtaining the basic potential flow solution used to obtain the imposed pressure required in Eq. (10) are well known and numerous, they are not discussed here. In this regard it should be noted that the basic tip vortex formation process can be obtained in the absence of any imposed pressure as was demonstrated by Govindan, Levy and Shamroth (Ref. 28). The present development concentrates on describing the numerical method used to solve the viscous primary/secondary equations. Streamwise derivative terms in the governing equations have a form such as $u_1 \partial(\ )/\partial x_1$, and because the streamwise velocity u_1 is very small in the viscous dominated region near no-slip walls, it is essential to use implicit algorithms which are not subject to stringent stability restrictions unrelated to accuracy requirements. Although it is possible to devise algorithms for the solution of the governing equations as a fully coupled implicit system, such algorithms would require considerable iteration for the system of equations treated here, and this would detract from the overall efficiency. The present method partitions the system of correction equations into subsystems which govern the primary flow, the secondary flow, and the turbulence model. This technique reduces the amount of iteration required and yet avoids the more severe stability restrictions of explicit algorithms. The primary-flow subset of equations contains the streamwise momentum equation. The secondary-flow subset of equations contains the secondary vorticity equation,

the scalar and vector potential equations and the pressure equation. These subsystems are decoupled using an ad hoc linearization in which secondary velocity components and turbulent viscosity are lagged and are solved sequentially during each axial step.

Summary of Algorithm

Physical approximations are made to the time-averaged Navier-Stokes equations to permit solution by a forward-marching algorithm. These approximations include specifying a nominal primary flow direction, neglect of diffusion in this specified direction, and the specification of the pressure gradient in the specified direction. The pressure gradient is taken from a potential flow solution for the flow. The resulting governing equations are rewritten with a change of variable resulting from the velocity decomposition of Eq. (5).

In the governing equations derivatives are replaced by finite-difference approximations. Three-point central difference formulas are used for all transverse spatial derivatives. Analytical coordinate transformations are employed as a means of introducing a nonuniform grid in each transverse coordinate direction, as appropriate, to concentrate grid points in the wall boundary layer regions. Second-order accuracy for the transverse directions is rigorously maintained. Two-point backward difference approximations are used for streamwise derivatives, although this is not essential.

As a first step in the procedure, a scalar ADI scheme is used for the momentum equation, Eq. (10). Given the solution for the primary flow, the secondary flow subsystem can be solved. First, the scalar potential equation (continuity), Eq. (8), is solved using a scalar iterative ADI scheme. Next, the secondary vorticity and vector potential equations, Eqs. (15) and (19) are written as a fully implicit coupled system and solved using an iterative linearized block implicit (LBI) scheme (cf. Briley and McDonald (30)). In selecting boundary conditions for the secondary flow subsystem, care must be taken to ensure that the final secondary velocity satisfies the no-slip condition accurately. Zero normal derivatives of ϕ are specified in the scalar potential equation, and this boundary condition corresponds to zero normal velocity. It is not possible to simultaneously specify the tangential velocity, however, and thus the ϕ-contribution to the

secondary velocity will have a nonzero tangential (slip) component, denoted v_t, at solid boundaries. In the coupled vorticity and vector-potential equations, both normal and tangential velocity components can be specified as boundary conditions, since these equations are solved as a coupled system. By choosing (a) zero normal velocity, and (b) $-v_t$ as the ψ-contribution to the tangential velocity, the slip velocity v_t arising from the ϕ calculation is cancelled, and the composite secondary flow velocity including both ϕ and ψ contributions will satisfy the no-slip condition exactly. The pressure equation (13) is solved using a scalar iterative ADI scheme.

A summary of the overall algorithm used to advance the solution a single axial step follows. It is assumed that the solution is known at the n-level x^n and is desired at x^{n+1}.

(1) The imposed streamwise pressure gradient distribution is determined from an a priori inviscid potential flow.

(2) The momentum equation is solved to determine u^{n+1}.

(3) Using values now available for ρ^{n+1} and u^{n+1}, the scalar potential equation (8) is solved using an iterative scalar ADI scheme, to obtain ϕ^{n+1}. This ensures that the continuity equation is satisfied.

(4) The equations for vorticity (15) and vector potential (9) form a coupled system for Ω^{n+1} and ψ^{n+1} which is solved as a coupled system using an iterative LBI scheme.

(5) Values for the transverse velocities v_s and w_s are computed from Eq. (3).

(6) The pressure is computed from Eq. (13).

RESULTS

Although the analysis previously described represents that which is currently used, the present effort was initiated prior to its full development. During early parts of the effort, a more approximate method was used. The major difference was use of an approximate no-slip condition in the secondary flow velocity components since at this stage of the development the coupled vorticity-stream function solver was not available. In this early work at any streamwise station the solution to the equations yielded a secondary flow slip velocity and the no-slip condition was obtained through a semi-empirical correction. Details of this as well as other items such as boundary conditions are given in Ref. 27. In this report calculations presented in Figs. 4-8 contain the semi-empirical correction to approximate the secondary flow no-slip condition. Figures 9-22, and the Concluding Remarks section of this report are based on calculations which use the rigorous no-slip condition at the rotor surface.

Initial Results Demonstrating Feasibility of this Approach

The initial portion of the program has been reported in Ref. 27 and for completeness is reviewed here. The results considered a constant thickness slab airfoil of rectangular planform immersed in a free stream at incidence of 6°. The Reynolds number is 10^6 based on chord. Although the configuration is an approximation, it represented a viable test case for an initial assessment of the procedure without the added complexity of body-fitted coordinates fitting the contoured airfoil. The pressure distribution used was obtained from calculations of Maskew (Ref. 16) and furnished by NASA Langley Research Center. The initial effort focused upon two problem areas; these were an analysis of the detailed tip vortex generation process and a qualitative comparison of the computed results with experimental data. A sketch indicating the coordinate system used is given in Figs. 1 and 2.

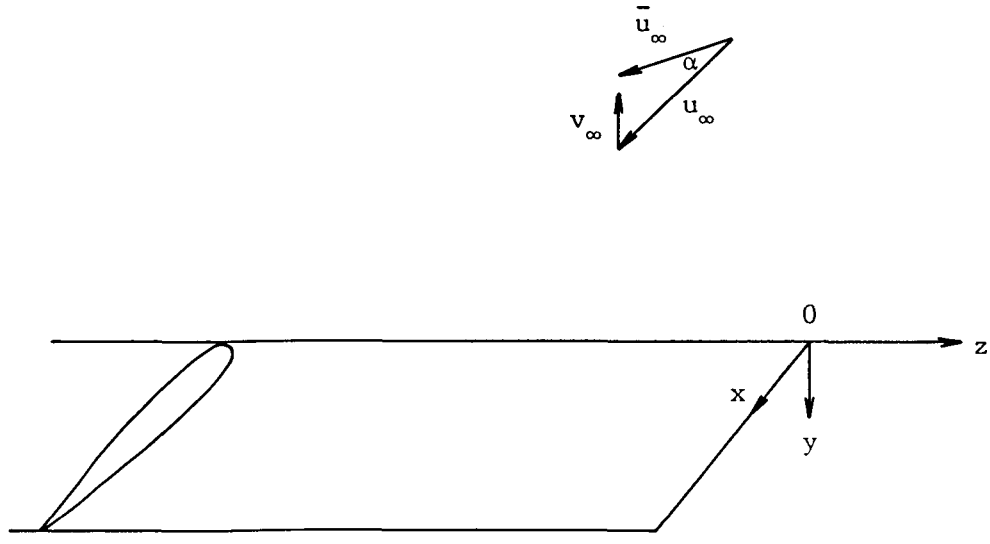

Figure 1. - Sketch of coordinate system.

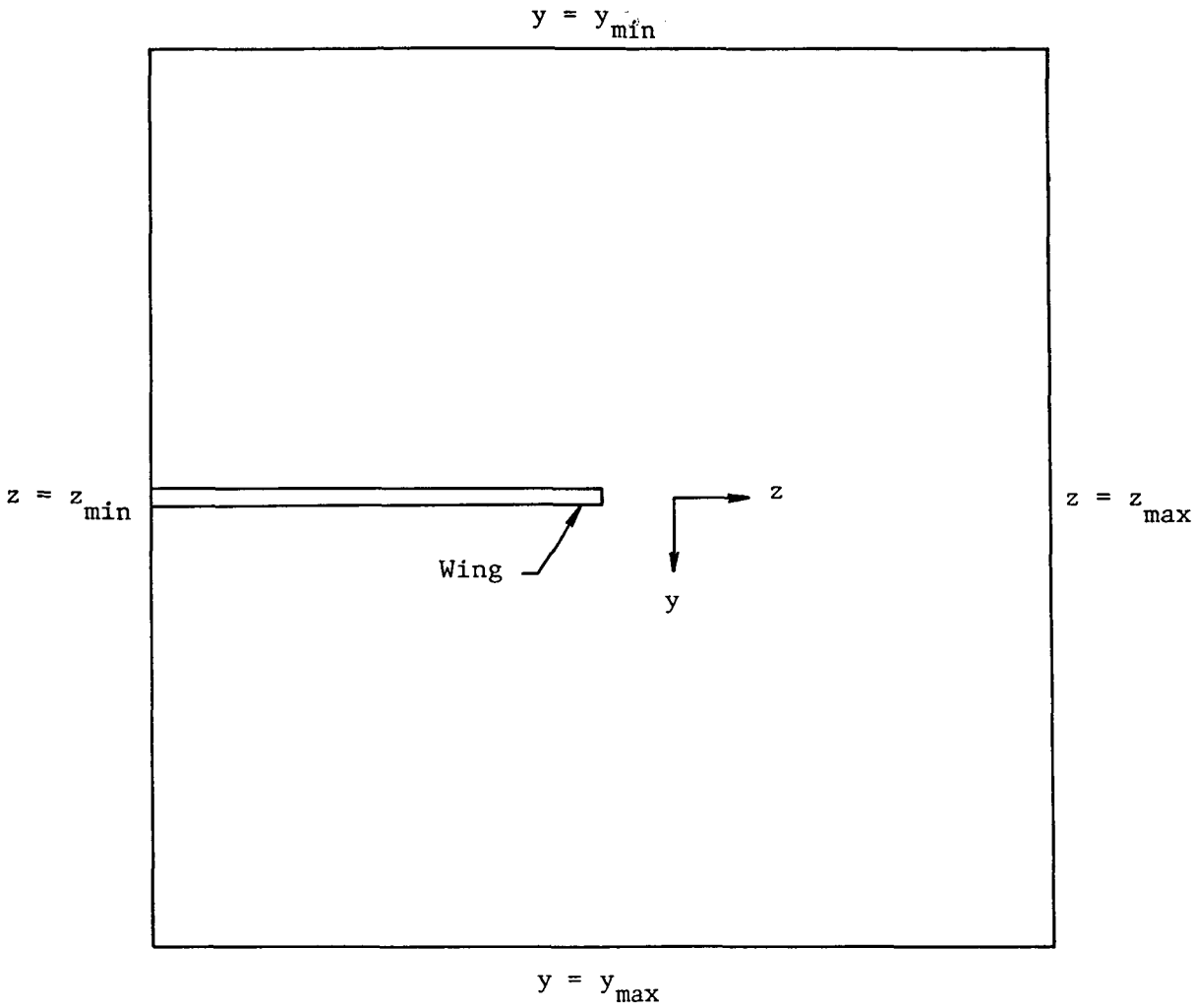

Figure 2. - Grid boundaries

Computational Grid

The computational grid in the cross flow plane was obtained via Roberts' transformations (Ref. 31) in both the transverse, y, direction and the spanwise, z, direction. The line defined by y = 0, z = 0 (the x-axis) was taken to lie at the intersection of the x-y plane coinciding with the airfoil tip location and the x-z plane coinciding with the airfoil centerplane location as shown in Figs. 1 and 2. The Roberts' transformation was performed so as to concentrate x-y planes in the vicinity of the airfoil tip and x-z planes in the vicinity of the airfoil surface. The cross-sectional computational plane was constructed as a 19 x 19 grid with points located at the following locations.

TABLE I. - Secondary Plane Grid Point Locations

Pt. No.	1	2	3	4	5	6	7
y/c or z/c	-.25	-.193	-.141	-.098	-.065	-.041	-.024

Pt. No.	8	9	10	11	12	13	14
y/c or z/c	-.012	-.005	0	.005	.012	.024	.041

Pt. No.	15	16	17	18	19
y/c or z/c	.065	.098	.141	.193	.25

The wing thickness was taken to be 0.01c; i.e., the wing was taken to be three grid points thick. In the streamwise direction a nonuniform grid which concentrated points in the airfoil leading edge region was used. The streamwise grid points were located as follows:

TABLE II. - Streamwise Grid Point Locations

Pt. No.	1	2	3	4	5	6	7
x/c	-0.1	-0.05	0.01	0.02	0.03	0.04	0.05

Pt. No.	8	9	10	11	12	13	14
x/c	0.07	0.09	0.11	0.13	0.15	0.19	0.23

Pt. No.	15	16	17	18	19	20	21
x/c	0.28	0.33	0.38	0.43	0.48	0.54	0.60

Pt. No.	22	23	24	25	26	27	28
x/c	0.65	0.70	0.75	0.80	0.85	0.90	0.95

where $x/c = 0$ is the location of the airfoil leading edge. The secondary flow plane grid points in the vicinity of the tip are shown in Fig. 3.

The calculation was initiated at $x/c = -0.1$ which is upstream of the airfoil leading edge. At the initial plane the streamwise velocity was set equal to the velocity predicted by the vortex lattice method and the streamwise vorticity was set equal to zero. Upon reaching the airfoil, no-slip conditions at the airfoil surface were applied to the streamwise momentum equation and this sudden application of the no-slip boundary did not lead to any numerical problems. In contrast, however, a special technique was required for the vorticity transport equation upon reaching the airfoil.

At the initial plane upstream of the airfoil, the vorticity was taken to be zero, and no vorticity is generated until the airfoil is reached. Rather than solve the vorticity transport equation at the first station at which the airfoil is encountered, the vorticity was assumed to be zero at this location. The stream function equation was solved, leading to a prediction of an irrotational secondary flow field which has a significant spanwise slip velocity. A boundary layer correction was applied to this secondary flow which decreased the spanwise velocity to zero at the airfoil surface and generated streamwise vorticity. The streamwise vorticity generated in this manner was taken as the vorticity at the first streamwise plane containing the airfoil; at subsequent streamwise locations the vorticity is determined from the vorticity conservation equation.

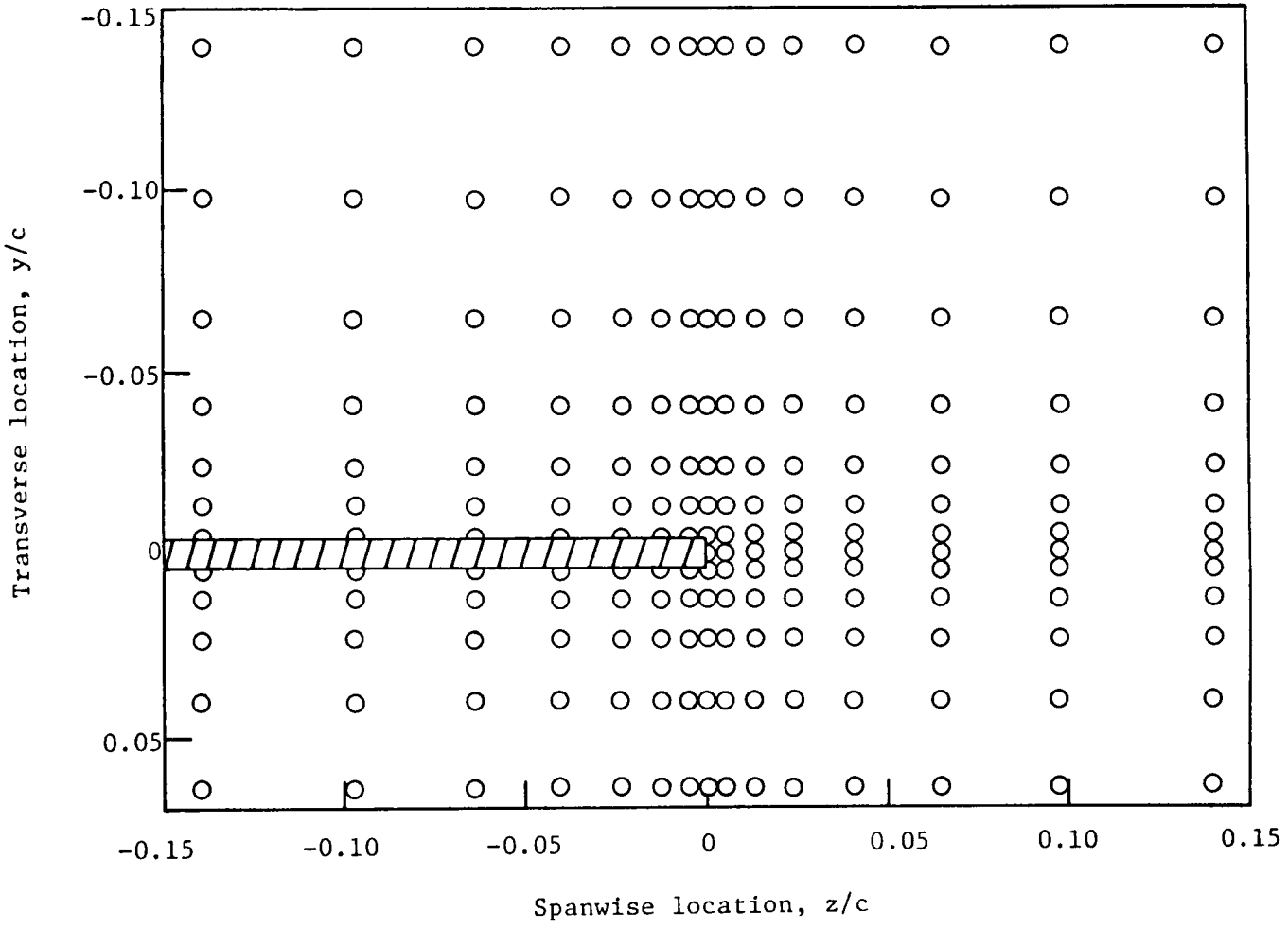

Figure 3. - Grid point locations in vicinity of tip.

The calculation was initiated as a constant viscosity flow with the viscosity being equal to the expected wall region eddy viscosity and transition to the usual simple eddy viscosity was assumed to occur at $x/c = 0.19$. Downstream of $x/c = 0.19$ a simple eddy viscosity model was used.

Turbulence Model

Since most airfoil flows of practical interest are in the turbulent regime, it is appropriate to include a turbulence model in the formulation. The eddy viscosity model used in the present effort assumes an eddy viscosity distribution throughout the boundary layer of approximately parabolic form with the maximum eddy viscosity being set as a function of the displacement thickness Reynolds number as suggested by Clauser (Ref. 32). According to Clauser, the maximum value of eddy viscosity is given by

$$\frac{\epsilon_{MAX}}{\nu} = 0.016 \frac{u_e \delta^*}{\nu} \tag{19}$$

The distribution within the boundary layer is taken as the following function of y/δ where δ is the boundary layer thickness.

$$\begin{aligned} \epsilon &= \epsilon_{MAX}(y/\delta) && y/\delta \leq 0.2 \\ \epsilon &= \epsilon_{MAX} && 0.2 \leq y/\delta \leq 0.5 \\ \epsilon &= \epsilon_{MAX}\left[1 - y/\delta\right]/0.5 && 0.5 \geq y/\delta \leq 1.0 \\ \epsilon &= 0 && y/\delta \geq 1.0 \end{aligned} \tag{20}$$

It should be noted that with this eddy viscosity model, turbulent viscosity is limited to regions in which the streamwise boundary layer is present. This is clearly a simplification and, as is commented upon subsequently, will give low values of vorticity diffusion. It should be

noted that the three-dimensional forward marching procedure has been used in conjunction with a two-equation turbulence model in Ref. 25, and such a model could be incorporated in the tip vortex version of this computer code.

The Predicted Tip Vortex Generation Mechanism

The results reported in Ref. 27 fall into two categories; (i) detailed numerical predictions and (ii) a qualitative understanding of the tip vortex generation mechanism. Since an understanding of the generation mechanism may aid the reader in understanding the detailed results for the cases which follow, this generation mechanism, as calculated by the analysis, is discussed first. Upon encountering the wing at incidence, the inviscid potential flow generates a pressure field leading to high pressures below and low pressures above the airfoil. Obviously, as the tip itself is approached, the pressures on the upper and lower sides must become equal. The pressure imbalance, thus generated, drives an irrotational flow in the secondary flow plane from the pressure side outboard, around the tip and finally inboard on the suction side. This secondary flow pattern is required to obey the no-slip condition at the airfoil surface and this no-slip condition generates positive vorticity on both the upper and lower surfaces. Due to the secondary flow pattern, the vorticity generated on the pressure surface is convected outboard and the vorticity generated on the suction surface is convected inboard.

As the flow proceeds downstream, the vorticity generated on the pressure surface is convected to the tip, shed off the tip and convected and diffused in a general upward and inboard direction. At some streamwise location the amount of positive vorticity appearing above the suction surface is sufficient to create a counterclockwise, circular, secondary flow velocity pattern above the suction surface; such that the spanwise velocity in the immediate vicinity of the airfoil suction surface is then directed outboard. However, since the no-slip condition must be satisfied, a region of negative vorticity appears adjoining the tip suction surface.

At approximately the same streamwise location, the positive vorticity which as been shed from the pressure surface and convected upward forms a "tongue-like" region of free vorticity above the suction surface and clearly distinct from the cross flow boundary layer. As is shown subsequently in

the present slab airfoil calculation, the appearance of this free vorticity occurred following the appearance of the negative vorticity region. These results are in qualitative agreement with the experimental evidence of Francis and Kennedy (Ref. 4) for the tip vortex generation process.

Detailed Results

The results of the calculation procedure are shown in Figs. 4-8. Due to the scarcity of experimental data, it is difficult to make a definitive assessment of the prediction at the present time; however, the data of Chigier and Corsiglia (Ref. 6) and Francis and Kennedy (Ref. 4) can be used for guidance. The data of Ref. 6 were taken for a NACA 0015 airfoil, immersed in a fluid at chord Reynolds number of 9.5×10^5, and at an incidence angle of 12°. The data of Ref. 4 were taken for a 46009 square tip, rectangular, untwisted airfoil section at 4° incidence. Although these conditions obviously differ from those of the case considered here, both cases represent high Reynolds number airfoils with rectangular planform tip shapes and both cases are for flows below the stall condition. Thus, the data of Refs. 4 and 6 can serve as a suitable qualitative guide for assessing the predicted results.

A summary of the computed results is presented in Fig. 4 which shows the vortex location and the maximum free vorticity magnitude. As is shown in Fig. 5, the streamwise vorticity consists of two parts; one portion is clearly associated with vorticity in the cross-flow boundary layers on both the suction and pressure airfoil surfaces. The second portion lies outside the cross flow boundary layers and results from vorticity shed at the airfoil tip; this is termed the free vorticity. Figure 4 shows the location of the center of the free vorticity as a function of streamwise distance; this location has been taken from Figs. 5.

As shown in the upper portion of Fig. 4, no definite free vortex appears until $x/c > 0.3$; upstream of this location, the vorticity appears to be concentrated in the boundary layers. After its appearance the core moves away from the airfoil surface and inboard. At the last station considered, the core is located at $y/c = -0.06$ and $z/c = -0.01$. The data of Ref. 6 for the NACA 0015 airfoil at 12° incidence show a vortex to appear first at $x/c \approx 0.25$; while that of Ref. 4 showed the vortex first to appear at

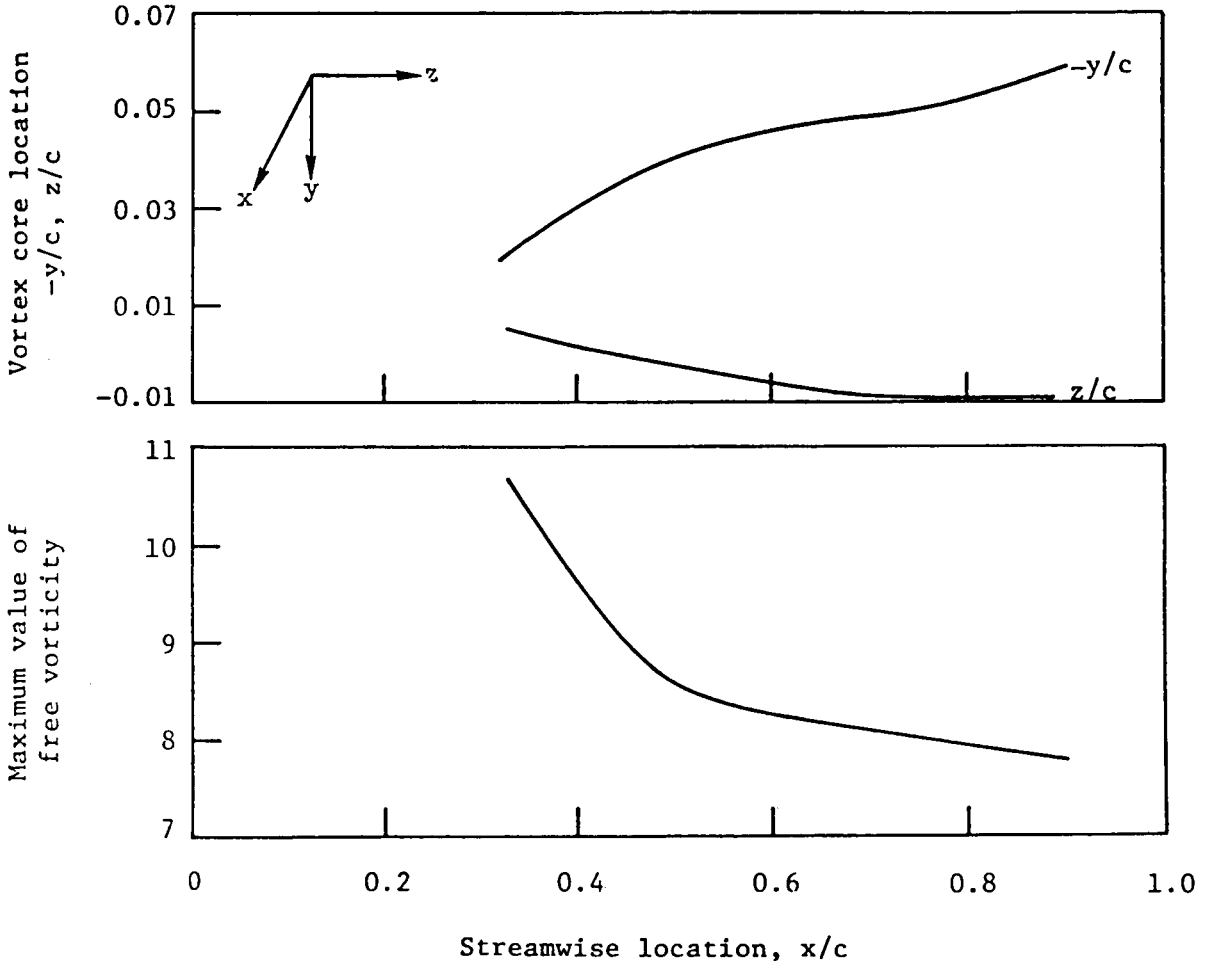

Figure 4. - Computed vortex development.

$x/c \approx 0.60$; these results are in reasonable agreement with the current prediction. The data then show the core to move away from the surface to a location $y/c \approx -0.09$, and inboard to a location $z/c \approx -0.05$. Although this data shows differences with the present prediction, particularly insofar as spanwise location is concerned, good qualitative agreement exists between the data of Ref. 6 and the predictions of the current analysis in terms of vortex location. Furthermore, in regard to the data of Ref. 6 since higher incidence angle will be accompanied by a stronger pressure differential from the pressure to the suction side of the airfoil, it is expected that higher incidence will produce a stronger flow around the airfoil tip; i.e., a secondary flow having both larger normal and spanwise velocity components. This stronger secondary flow would be expected to convect the shed vorticity both further above the airfoil and further inboard from the airfoil tip. Thus, the difference between the current prediction and the data of Ref. 4 is qualitatively as expected.

The lower portion of Fig. 4 shows the magnitude of the maximum vorticity appearing in the free vortex. As can be seen, this continuously decreases due to viscous effects which tend both to diffuse vorticity from regions of high to low vorticity concentration and to decrease the total amount of vorticity in the field. It should be noted that with the present turbulence model, the turbulent viscosity in the vortex core is underestimated and, hence, the diffusion of vorticity in the core region is also underestimated. The vorticity has been normalized by u_∞/c where u_∞ is the u component of velocity at upstream infinity and c is the chord.

Vorticity contours at selected streamwise stations are shown in Figs. 5. At $x/c = 0.11$ the streamwise vorticity is associated almost entirely with the cross flow boundary layers on the upper and lower airfoil surfaces and at the tip. The free stream is basically an irrotational flow field. The last laminar station is at $x/c = 0.19$. At this location there appears to be a concentration of positive vorticity in the tip region with some vorticity in the free stream and a small area of negative vorticity appears just above the airfoil surface for the first time. This appearance is explained as follows. The positive vorticity collecting above the suction surface in the tip region causes the free stream in this region to be rotational. This rotational free stream leads to a counterclockwise rotating fluid pattern above the suction surface. However, the fluid must obey the

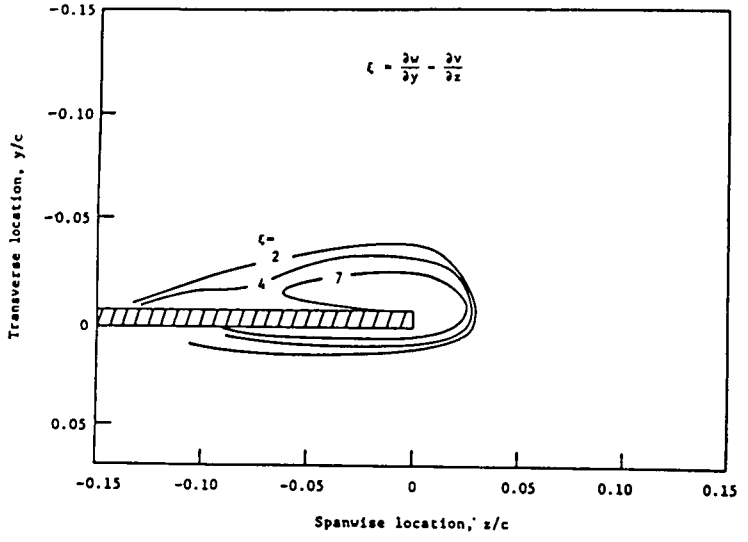

x/c = .11

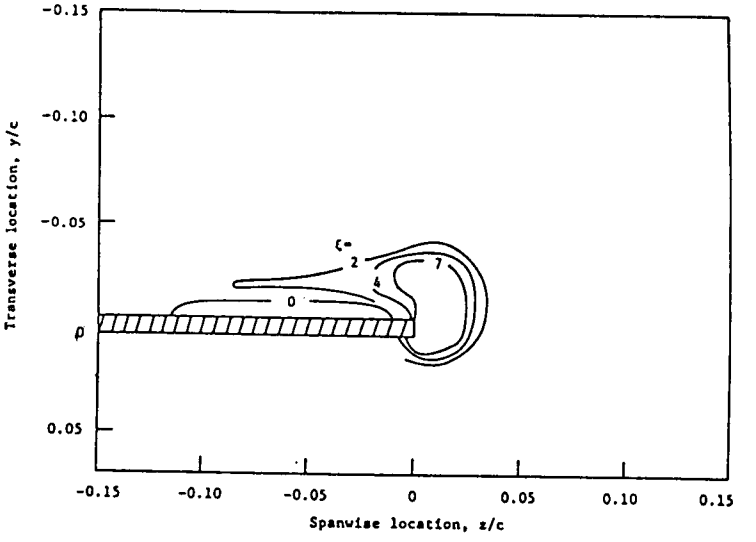

x/c = .19

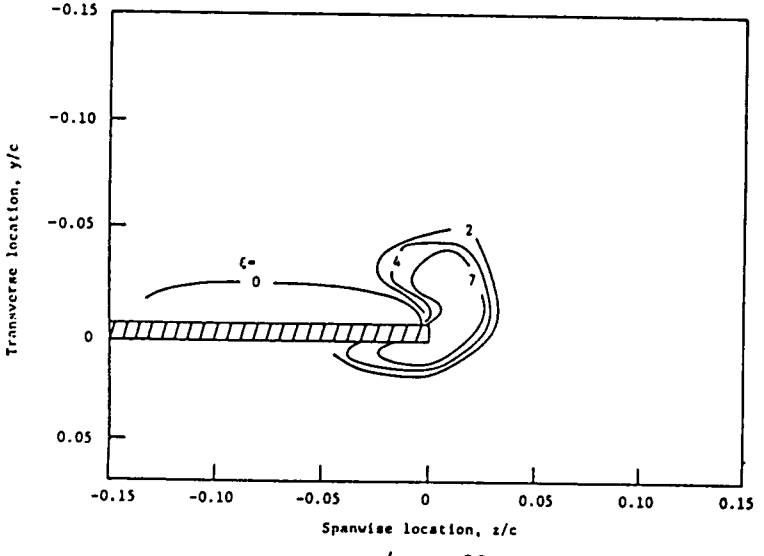

x/c = .33

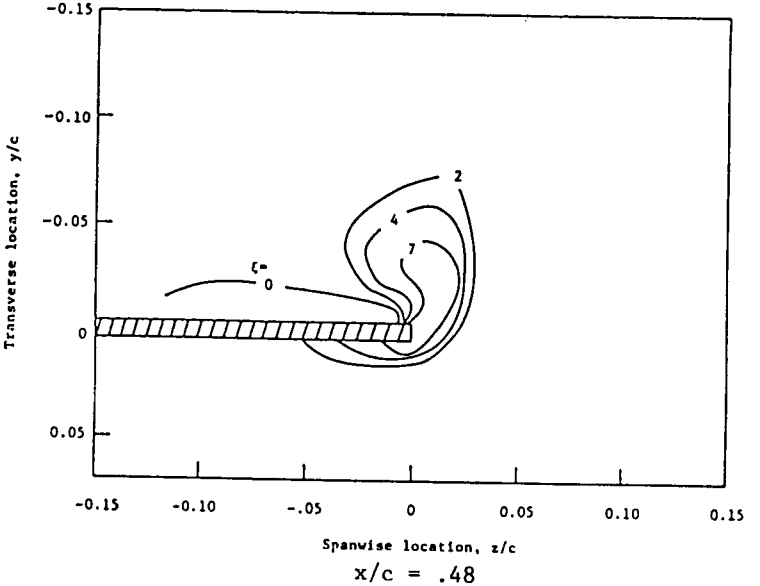

x/c = .48

Figure 5. - Vorticity contours

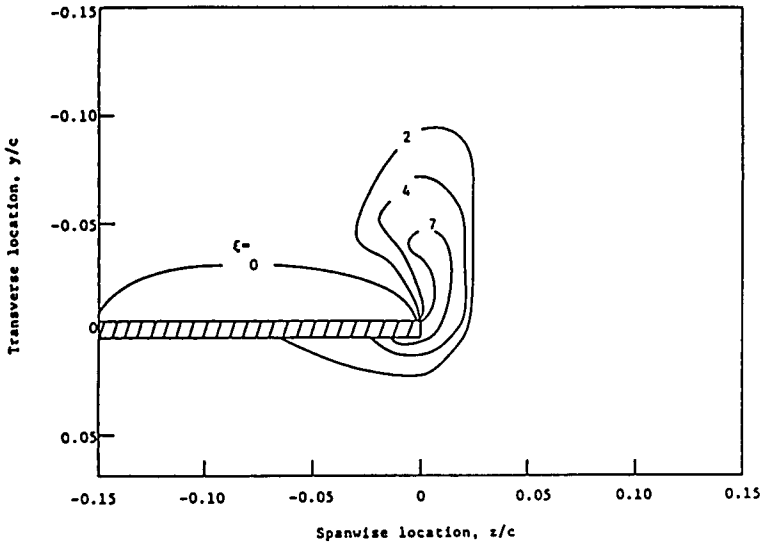

x/c = .60

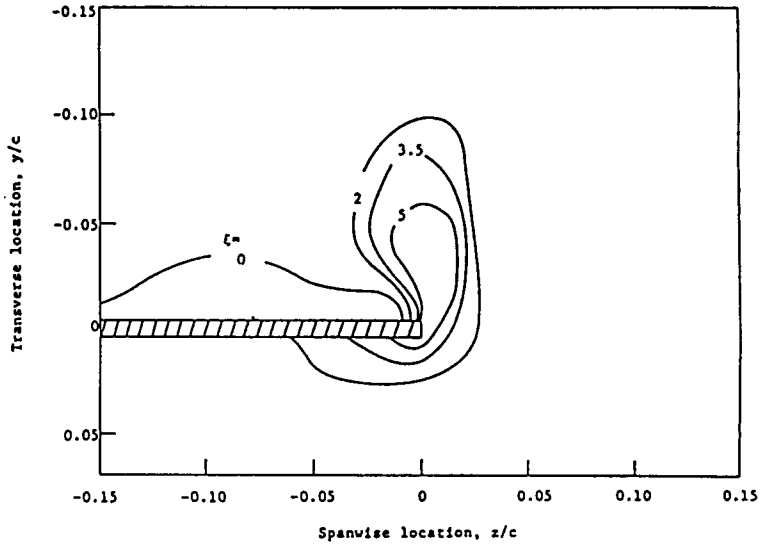

x/c = .75

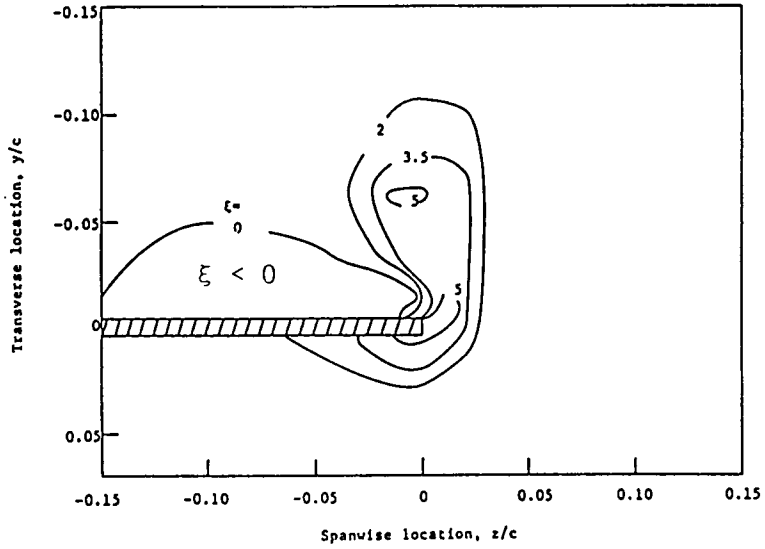

x/c = .90

Figure 5 (Concluded) - Vorticity Contours

no-slip condition on the airfoil surface and imposition of the no-slip condition to the secondary flow generates negative vorticity at the airfoil surface which then diffuses into the flow field. The net result is a flow pattern in which the spanwise flow is outboard below the airfoil. Above the airfoil the flow is inboard except in the immediate vicinity of the airfoil where it is outboard. The result is general convection of fluid around the tip from pressure to suction surface upon which is imposed a "circular" type of flow pattern above the airfoil and in the vicinity of the tip region. It should be noted that this negative vorticity is in a region of outward spanwise flow, and the possibility of the counter-rotating vorticity being carried outboard of the tip exists. Such a phenomenon has been observed experimentally as a secondary vortex.

The streamwise location $x/c = 0.19$ is the first location at which this "circular" flow pattern is evident, and this may be considered the location at which the vortex first appears. However, a more striking example of free vorticity is shown at $x/c = 0.33$. At this location, areas of strong vorticity are clearly being convected from the tip region above the airfoil and inboard. The general picture of the generation process being presented is the convection of the pressure surface cross flow boundary layer off the tip region, upward and then inboard. The pattern continues as the flow progresses to $x/c = 0.75$. From this location to the trailing edge the major effect appears to be the dissipation of vorticity and continued upward convection.

The possibility of the appearance of a secondary counter-rotating vortex has been mentioned previously and an examination of results at $x/c = 0.90$ shows appearance of such a region. As seen in this figure, a small region of negative vorticity has migrated via convection and diffusion processes to the immediate vicinity of the airfoil tip and may indicate the incipient formation of secondary vortex.

Contours of streamwise velocity are presented in Fig. 6. In general, these figures show the growth of the streamwise boundary layers. At inboard locations, the pressure surface boundary layers are thicker than the suction surface boundary layers; this result is consistent with the imposed pressure distribution obtained from the vortex lattice calculation and the two-dimensional boundary layers. However, in the tip region where the flow is strongly three-dimensional, the viscous region on the suction surface is thicker than that on the pressure surface.

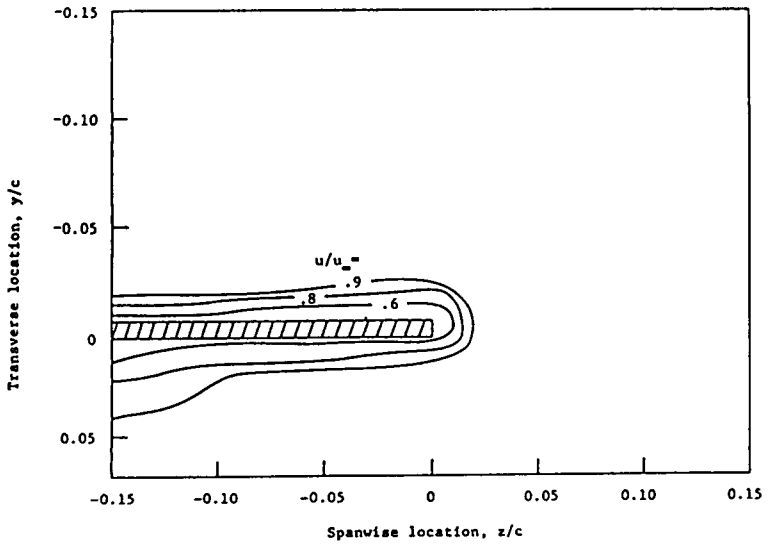

x/c = .11

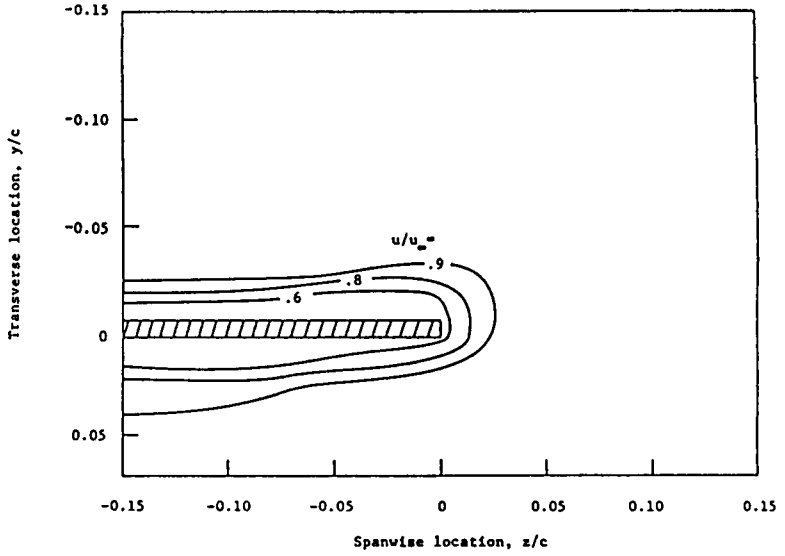

x/c = .19

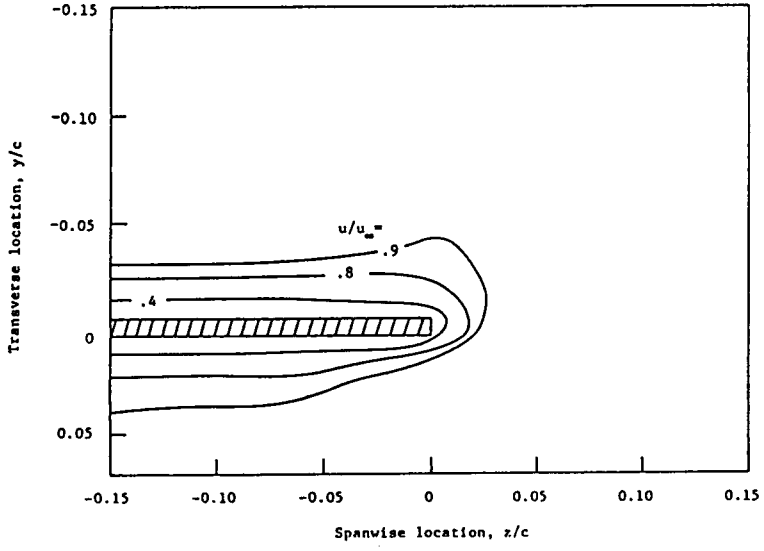

x/c = .33

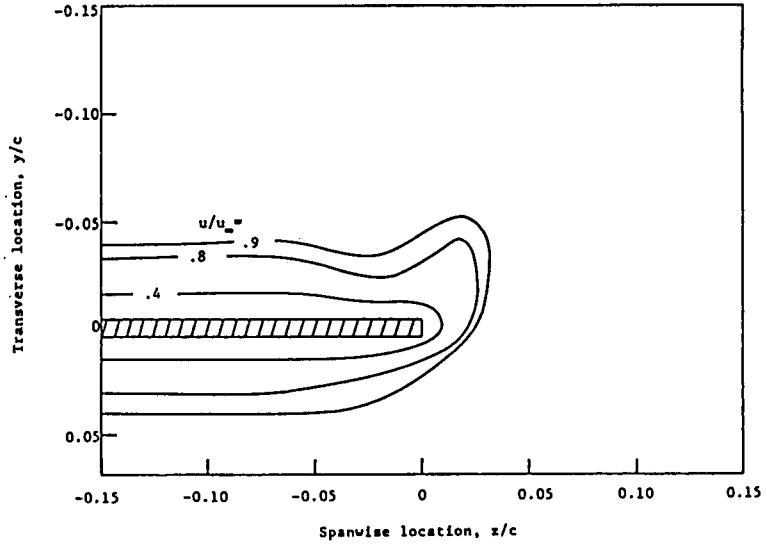

x/c = .48

Figure 6.- Streamwise velocity contours

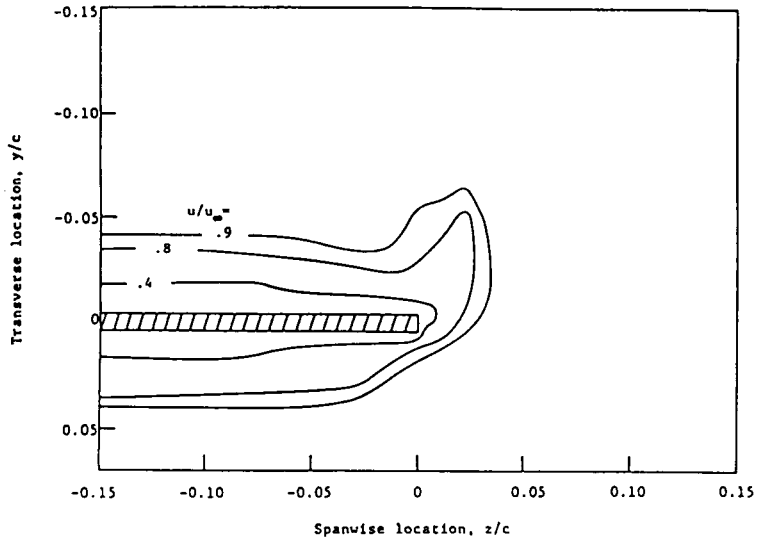

x/c = .60

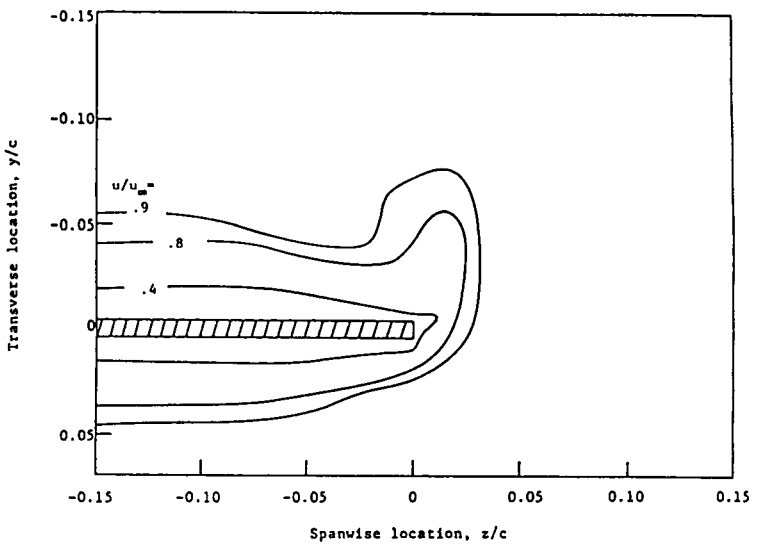

x/c = .75

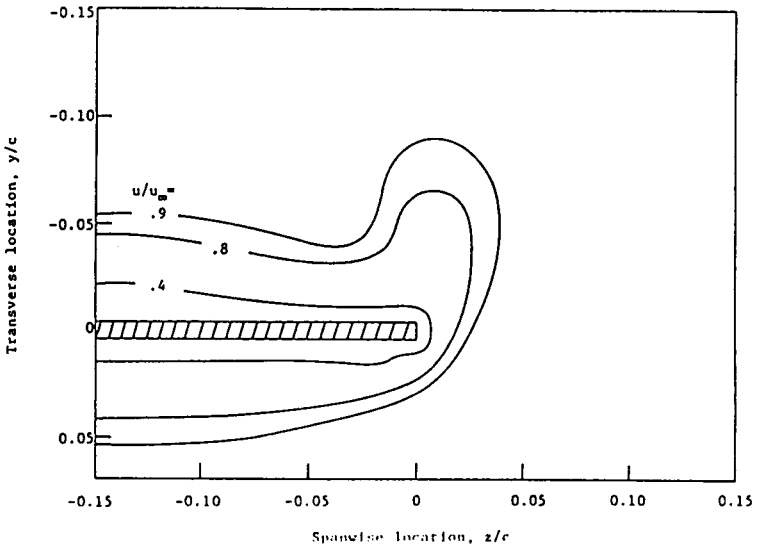

x/c = .90

Figure 6 (Concluded) - Streamwise velocity contours

As the flow proceeds downstream to x/c = 0.33, the major development is the expected thickening of the viscous layers. However, at x/c = 0.48 a new development appears. In the vicinity of the tip suction surface a thickening of the outer portion of the boundary layer appears. Although the contour with constant velocity 0.4 moves towards the airfoil surface indicating a thinning of the inner part of the boundary layer, the contour with constant velocity 0.9 moves away from the airfoil indicating a thickening on this part of the airfoil. This clearly shows a behavior not observed in usual two-dimensional boundary layers.

A set of plots showing secondary flow patterns predicted by the calculation is presented in Fig. 7. In these figures the secondary velocities are the spanwise velocity, w, and the velocity normal to the free flow stream velocity rather than the velocity normal to the airfoil. Thus, in the absence of no-slip effects, the value of v far from the surface would be approximately u sin α. (See the sketch on the figure). At x/c = 0.11, the vortex has not yet formed as the secondary flow pattern simply shows flow around the tip from the suction surface to the pressure surface. The next plot shows the vortex beginning to form at x/c = 0.19; this result is consistent with the vorticity plots and the core defined by the velocity plots at this station, if one exists, appears to be very close to the suction surface corner point. The remaining plots show the further development of the secondary flow vortex as well as the upward movement of core as defined by the velocity plots. At these latter stations the secondary flow shows a definite circular flow pattern; at x/c = 0.90 the secondary flow has an average circumferential velocity of approximately 0.06 u_∞. The measurements of Ref. 6 at the airfoil trailing edge show a tangential velocity of approximately 0.2 u_∞, however, the Ref. 6 data is for a higher angle of incidence (12° vs. 6°) and thus the generation of a stronger vortex in this case is to be expected.

Results indicating the predicted circumferential velocity profiles through the vortex core are presented in Fig. 8. In each case, the vortex core location was estimated from the velocity plots of Fig. 7 and the velocity distribution on a spanwise line through the core center was used to obtain the results. Since the present case is not for the same conditions as the data of Ref. 6 (the major discrepancy being 6° incidence angle in the present case and 12° incidence angle in Ref. 4), a quantative comparison

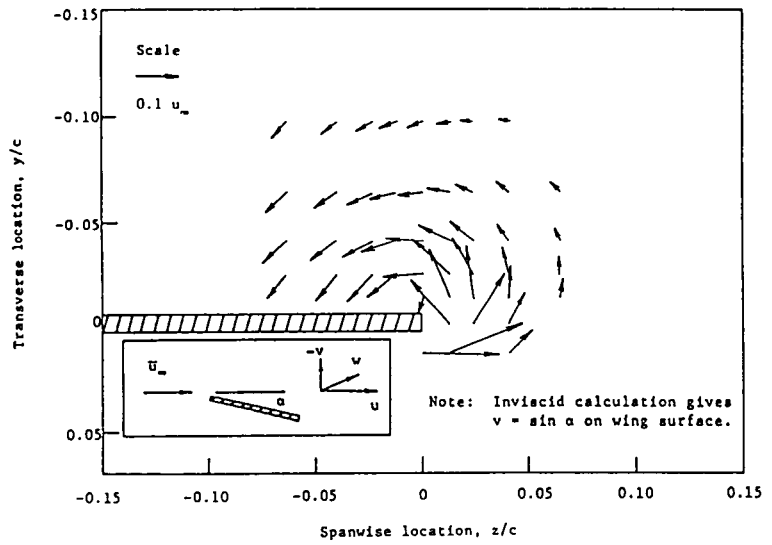

x/c = .11

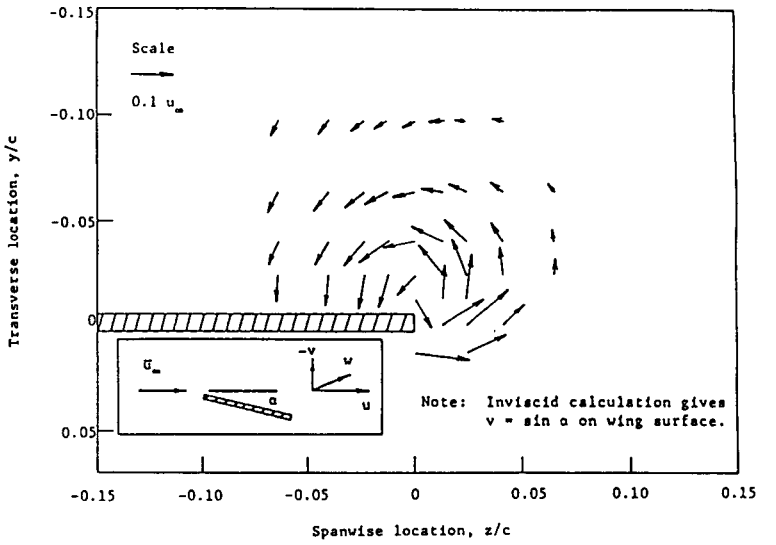

x/c = .19

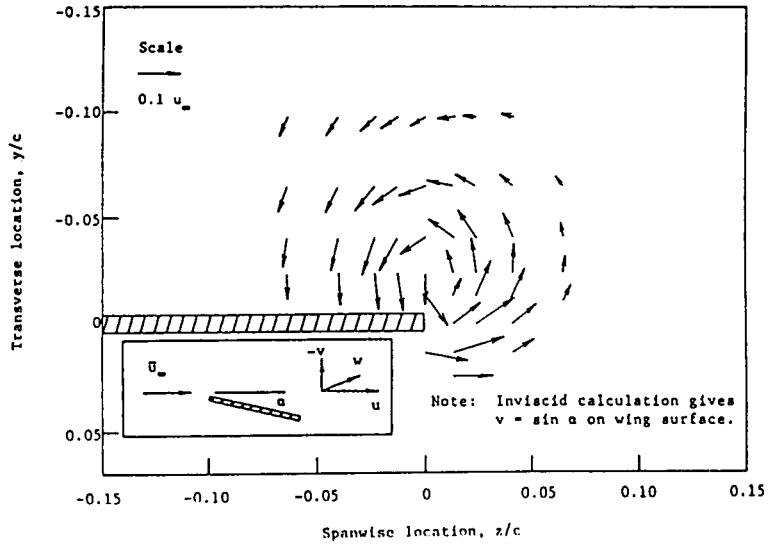

x/c = .33

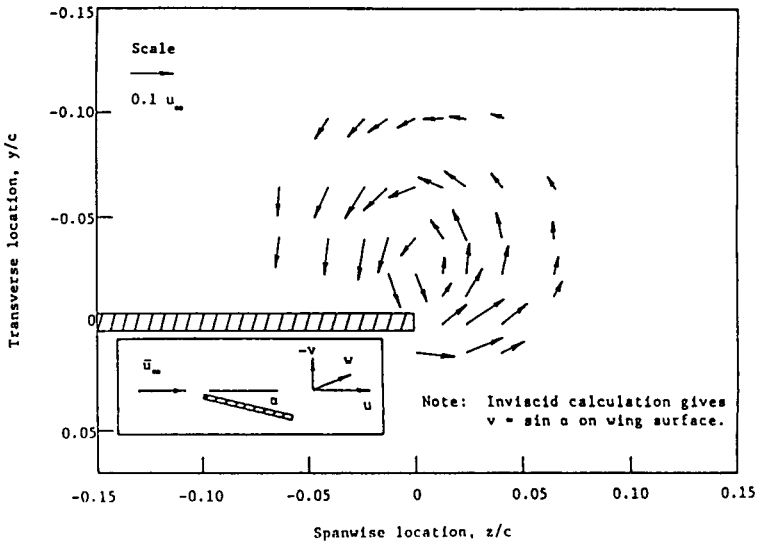

x/c = ..48

Figure 7. - Secondary velocity vector

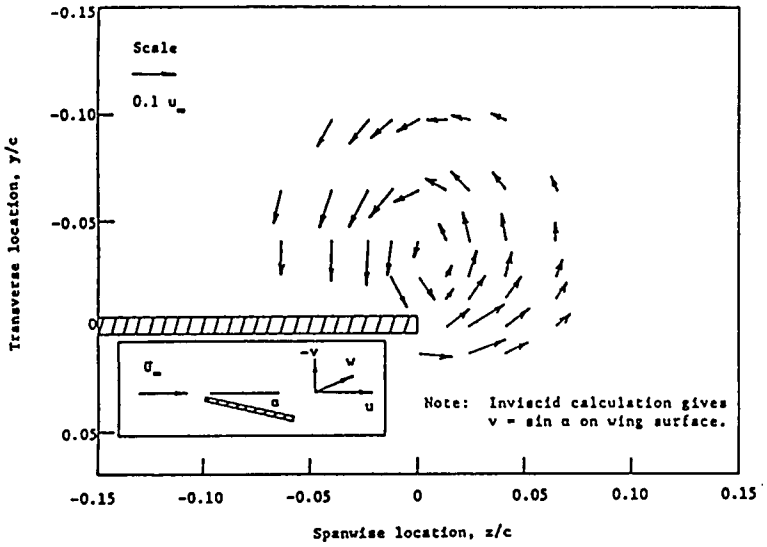

x/c = .60

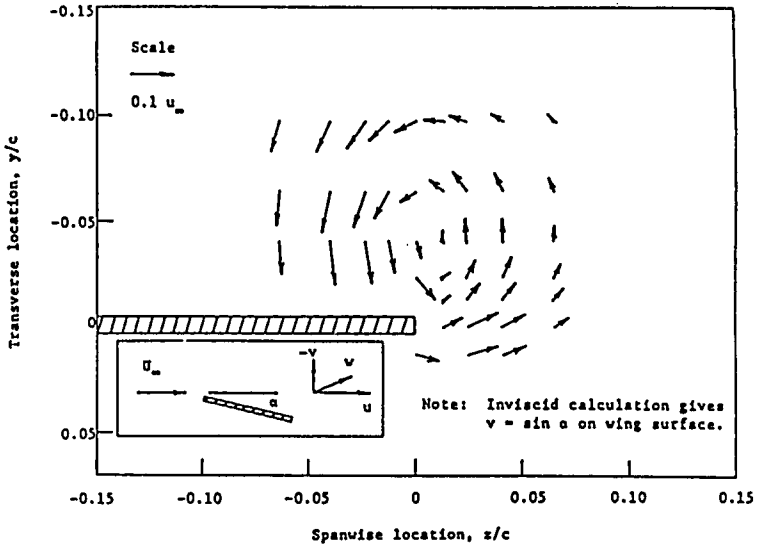

x/c = .75

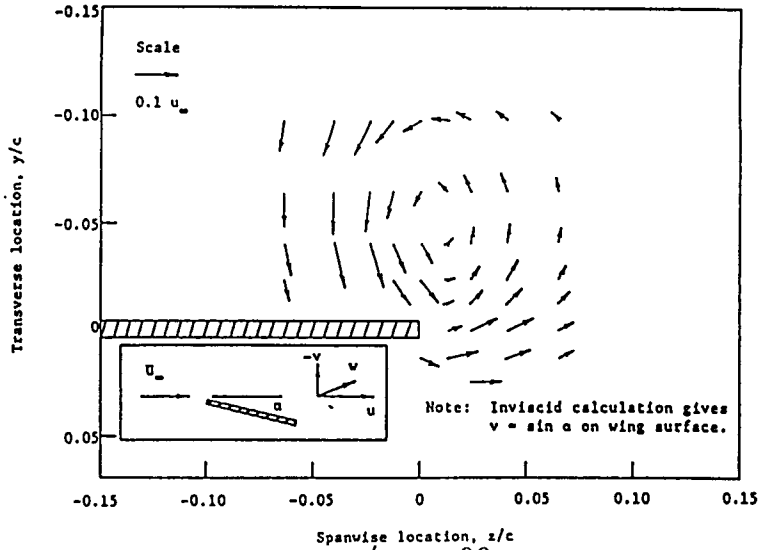

x/c = .90

Figure 7 (Concluded) - Secondary velocity vectors

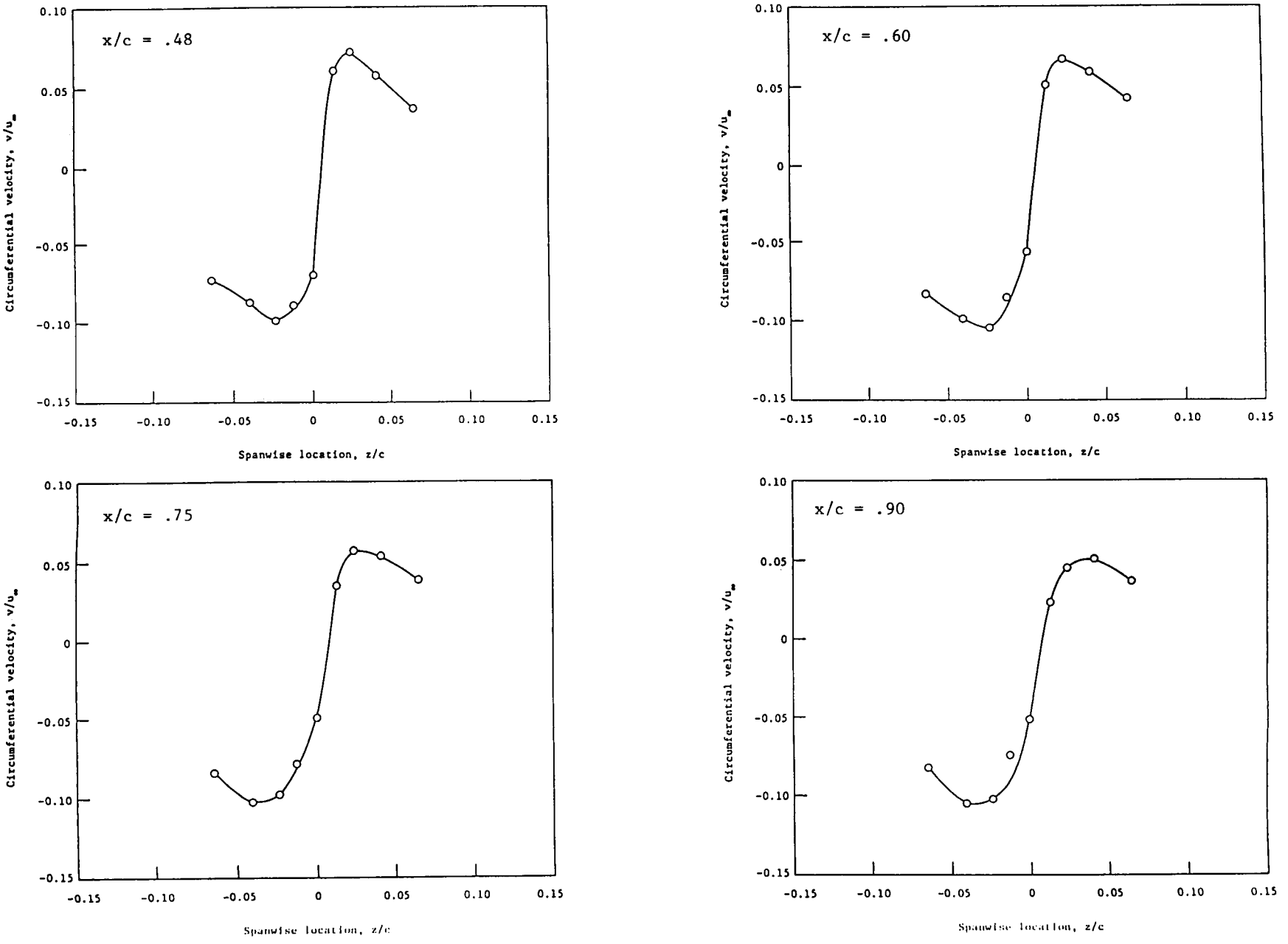

Figure 8. - Velocity distributions through vortex

between predictions and data cannot be made. Nevertheless, qualitative similarity between the two sets of results is apparent. In both cases, the vortex increases in size and the maximum tangential velocity decreases in magnitude as the flow progresses downstream. The data of Chigier and Corsiglia (Ref. 6) shows the core increasing from $r_c = 0.02$ at $x/c = 0.5$ to $r_c/c = 0.09$ at $x/c = 1.0$. The present results show an approximate factor of 2 increase in the size of the vortex core from mid-chord to the trailing edge.

Thin Slab No-Slip Secondary Flow Cases

Although the previous calculations clearly showed the basic tip vortex generation mechanism via three-dimensional viscous flow calculations, they did not generate zero-slip secondary flows from the basic equations. In these early calculations the zero-slip secondary flow relation was obtained via a correction procedure (Ref. 27). A new solution procedure which satisfies the no-slip condition on secondary flow was developed and the remaining calculations were done with this rigorous no-slip condition satisfied.

The first of these calculations were thin slab calculations for both laminar and turbulent flow. The cases considered were for 5° incidence at Mach numbers of 0.01, and Reynolds numbers of 2×10^3 and 10^6, respectively. Since the laminar case and turbulent calculations showed basically the same physical processes only the turbulent case is included in this final report.

The potential flow field for this case was obtained from NASA Langley Research Center from implementation of the procedure due to Maskew (Ref. 16). A 59 by 49 cross section grid with a sinh transformation to concentrate grid points in the vicinity of wall and tip regions is used. There are 20 streamwise stations in the streamwise direction. The viscous calculation was started downstream of the leading edge of the wing at $x/c = 0.05$ where x is the streamwise coordinate measured from the leading edge and c is the wing chord. The initial boundary layer thickness for this demonstration case was taken as $\delta/c = 0.07$. Figure 9 presents the streamwise vorticity at the 11% chord location. At this station the vorticity is contained deep within the streamwise boundary layer. The region of high vorticity at the wing tip is the result of the flow from the pressure surface

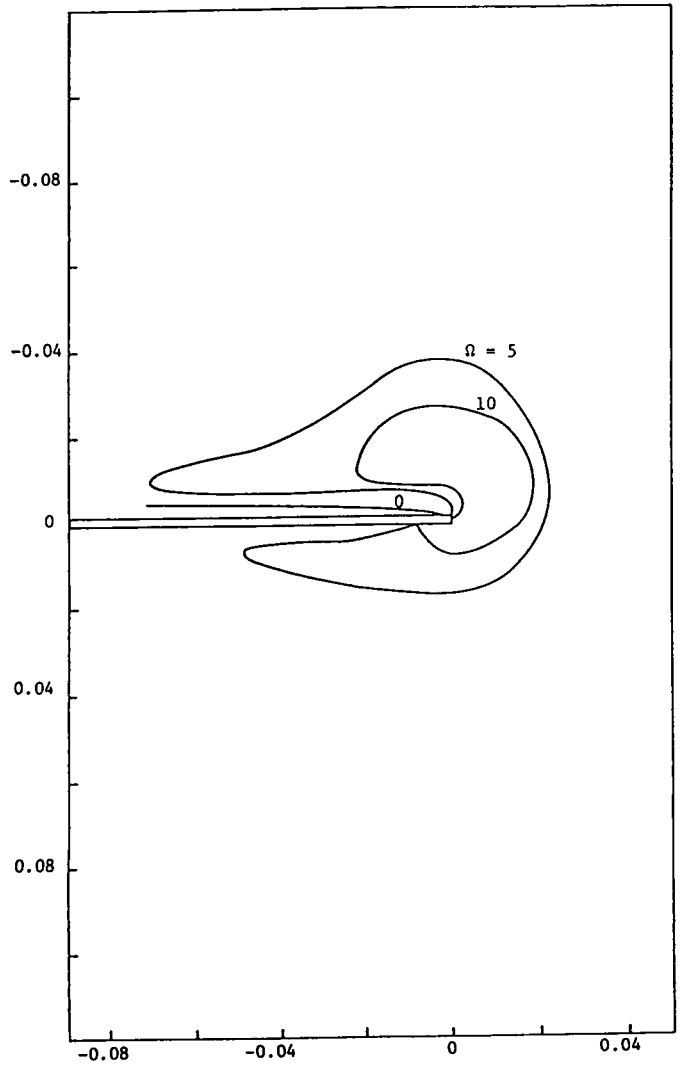

Contours of Constant Vorticity, x/c = 0.11

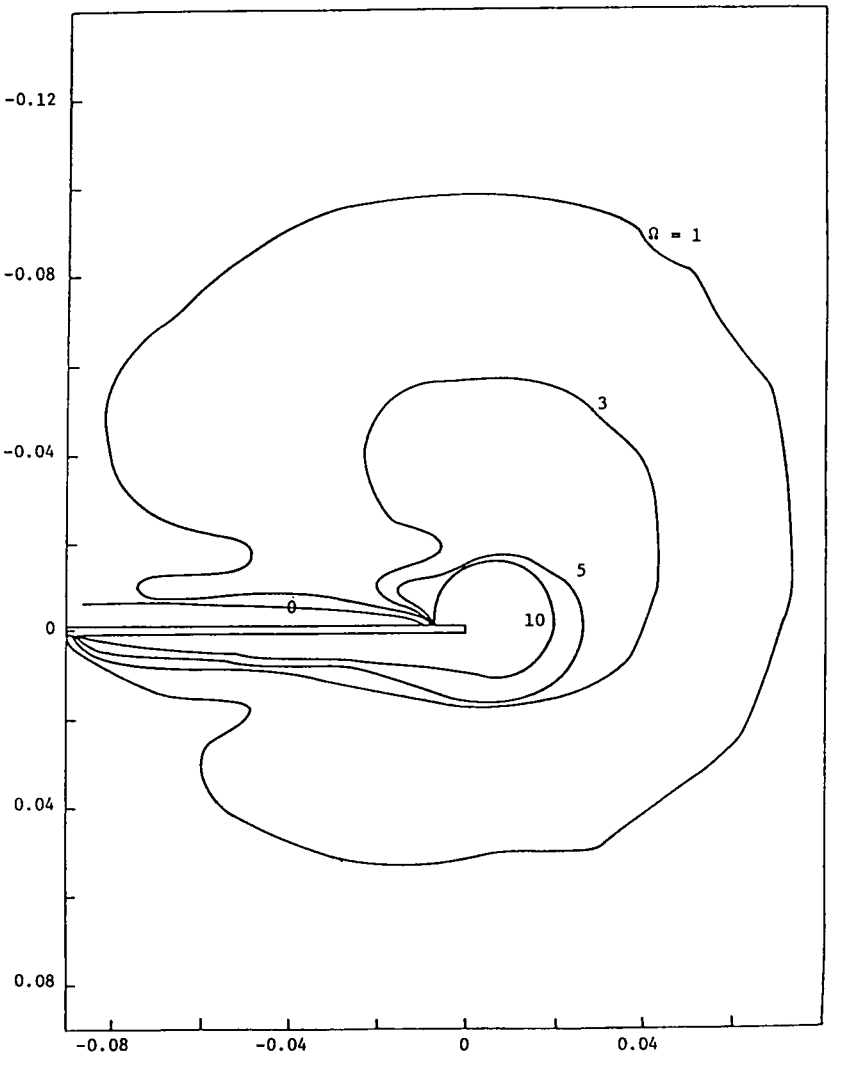

Contours of Constant Vorticity, x/c = 0.31

Figure 9. - Vorticity contours

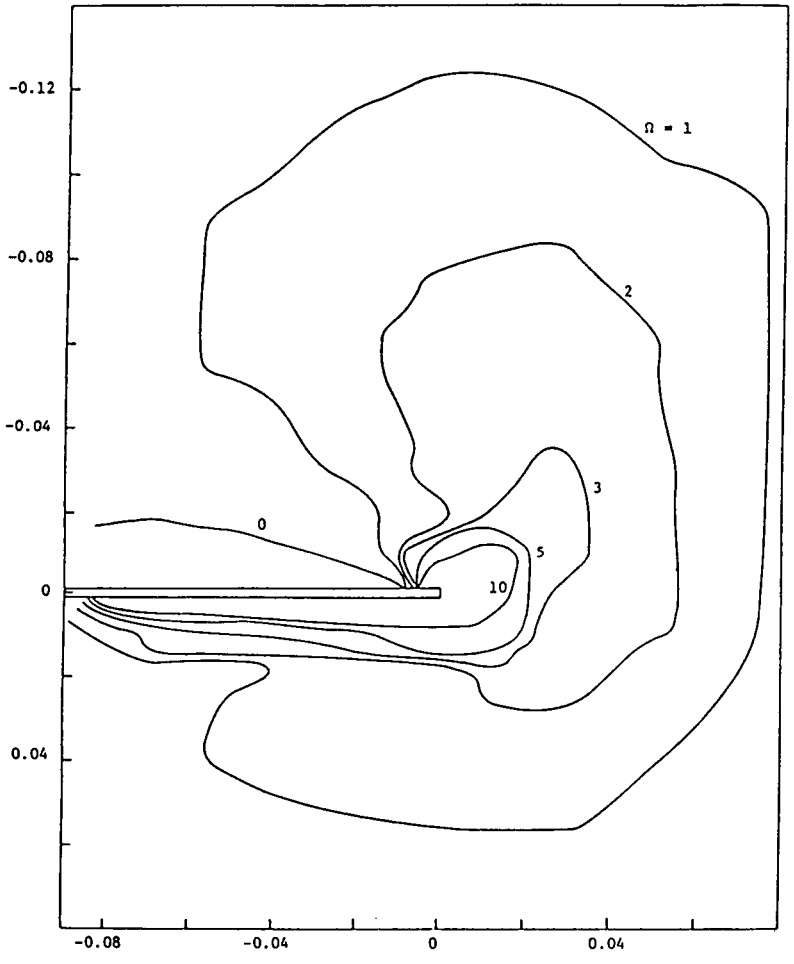

Fig. - Contours of Constant Vorticity, x/c = 0.59

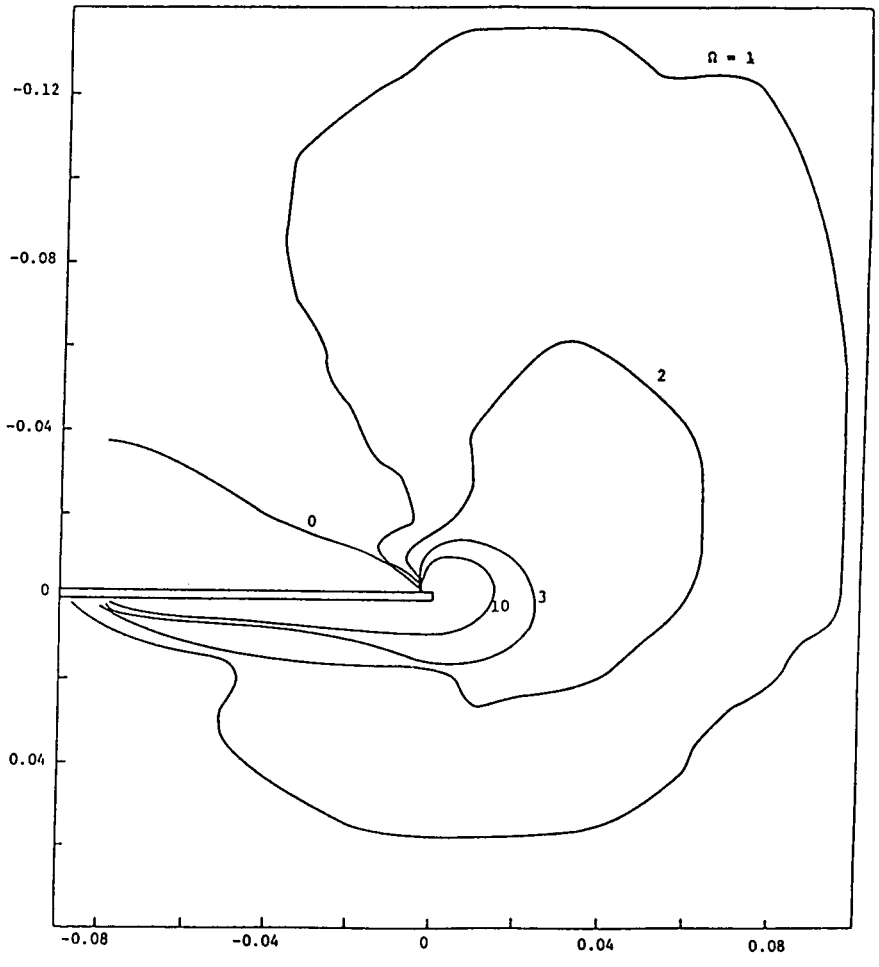

Fig. - Contours of Constant Vorticity, x/c = 0.81

Figure 9 (Concluded) - Vorticity contours

to the suction surface. Further downstream, the vorticity from below the wing tip is convected above the wing as shown progressively in Fig. 9. As the region of positive vorticity moves above the wing tip a large scale vortex pattern of secondary flow is established. The flow from this vortex is outward along the upper surface of the wing. Bringing this secondary flow to no-slip at the wing results in a region of negative vorticity along the upper wing surface. The region of negative vorticity is defined by the $\Omega = 0$ contour in Fig. 9, and is shown to get progressively larger as the secondary flow becomes stronger. Figure 10 shows the secondary flow velocity pattern at stations $x/c = 0.31$ and $x/c = 0.91$.

As can be seen, the generation process with the revised formulation which specifically sets zero no-slip on the wing is qualitatively similar to that previously obtained. The formation of the vortex above the surface and its migration slightly inboard as noted in Fig. 9 is in qualitative agreement with the previously obtained results, and the generated secondary flow pattern can be clearly seen in Fig. 10.

Constant Thickness Rounded Tip

The next case considered focused upon a constant slab wing with a rounded tip. The coordinate system for this calculation is a body-fitted curvilinear wing tip coordinate system developed by Thames (Ref. 33). This calculation represents a significant increase in complexity from the square tip calculations discussed previously. The coordinates used are general nonorthogonal rather than Cartesian and, therefore, the case demonstrates a much more general coordinate capability. A second item concerns the rounded tip. In the previous calculations, secondary flow separation is triggered by the sharp corners at the tip of the airfoil cross-section. In the present calculations, the secondary flow can separate any place on the rounded tip. Since this new case represented considerable additional complexity, a sample calculation for a constant thickness wing was chosen as a demonstration calculation.

The case presented here is for laminar flow over a thin wing with rounded tip and constant thickness at 5° angle of attack. The Reynolds number based on chord is 2000 and Mach number is 0.01. The initial boundary layer thickness is $\delta/c = 0.07$. The body-fitted curvilinear wing tip

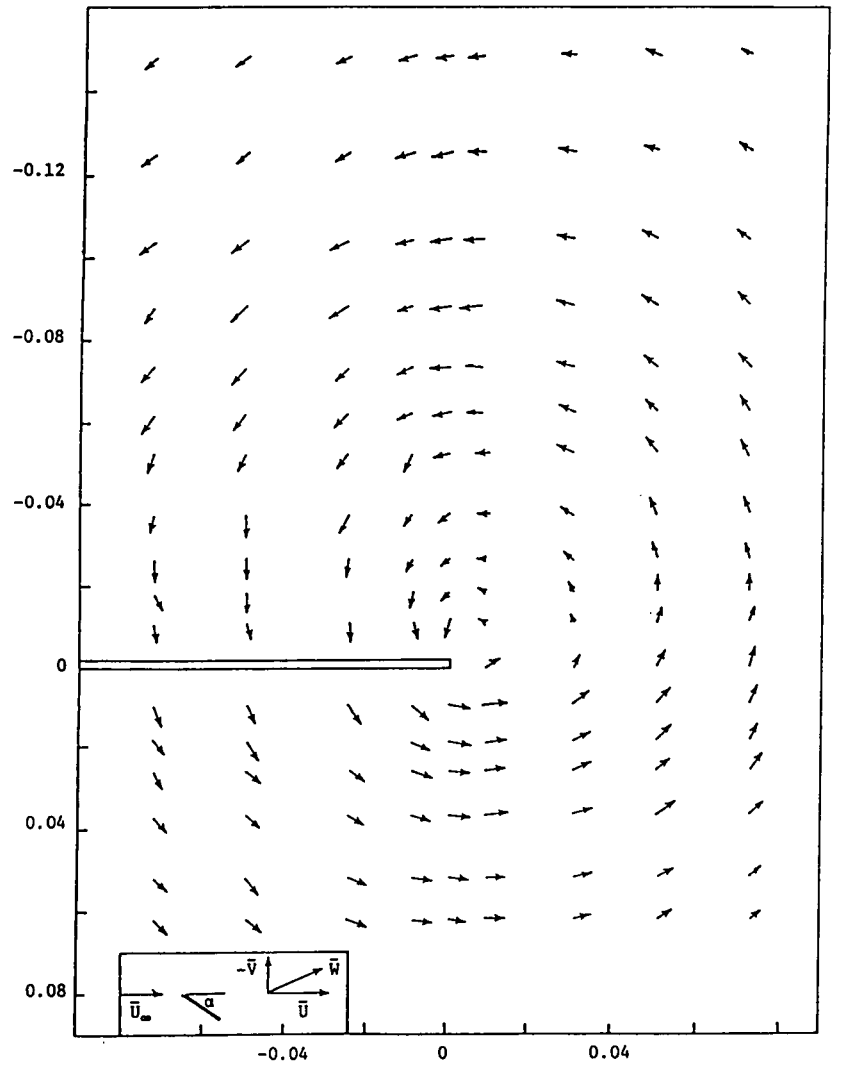

Fig. - Secondary Velocity Contours, x/c - 0.31

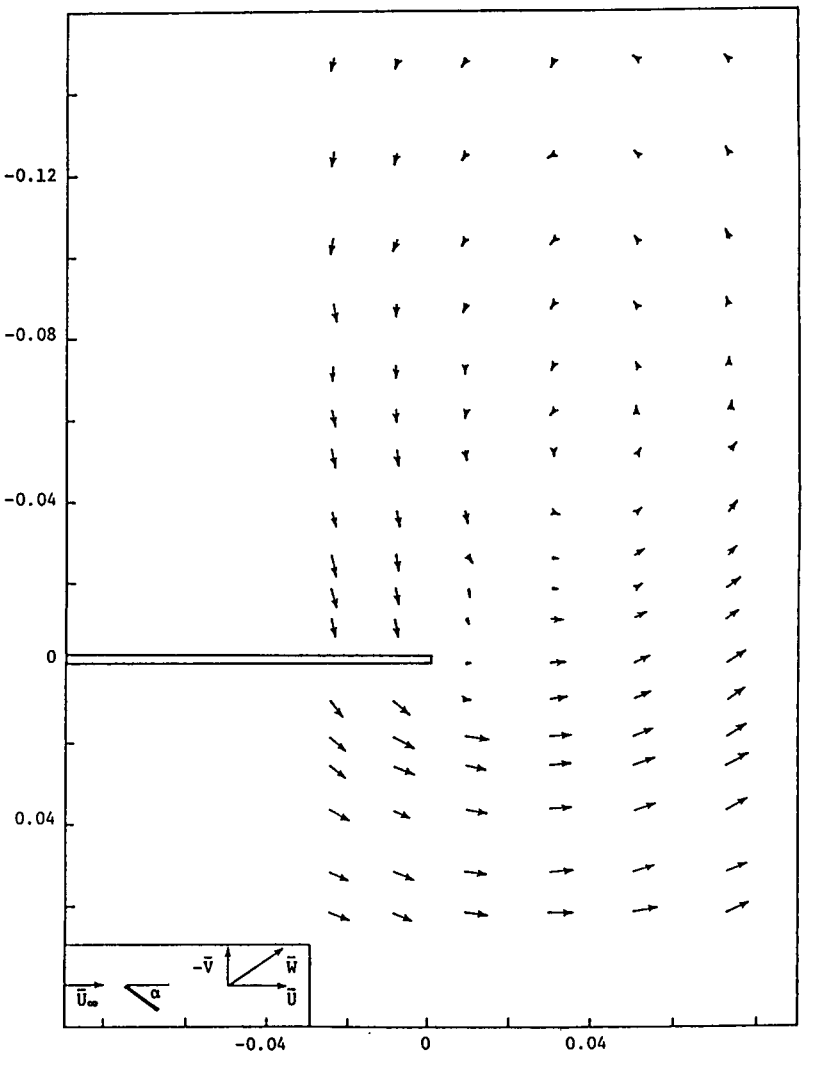

Fig. - Secondary Velocity Contours, x/c = 0.81

Figure 10. - Secondary velocity vectors

coordinate system was developed for a NACA 0012 airfoil. For the present constant thickness wing case, the cross-sectional grid was obtained from one cross-section of general three-dimensional grid and this was held the same in the downstream direction. There is 30 x 33 grid points in the cross section, and 20 grid points in the streamwise direction. The potential flow pressure field was provided by NASA Langley Research Center and was obtained from the calculation procedure of Maskew (Ref. 16).

Figure 11 presents the contours of streamwise velocity. Note that in Figs. 11-21 the suction surface is pictured on the right side of the blade and the pressure surface on the left. Although the initial station streamwise velocity is two-dimensional (except near the tip), the streamwise velocity is progressively distorted and shows strong three-dimensional features as the flow progresses downstream. Figure 12 shows the streamwise vorticity at the 25% chord location. At this station the vorticity is contained within the streamwise boundary layer. The region of high vorticity at the wing tip is the result of the flow from the pressure surface to the suction surface. Further downstream, the vorticity from below the wing tip is convected above the wing and the region of significant streamwise vorticity becomes larger, as shown in Figs. 12. However, the maximum vorticity magnitude becomes smaller due to viscous effects. Figures 13 show the secondary flow patterns at stations x/c = 25%, 39% 64% and 89%. These results clearly show the development of the tip vortex, and the distinct secondary flow pattern. The general development appears to be qualitatively similar to that obtained for the square tip.

Wing with an NACA 0012 Airfoil Section

Following the rounded tip calculation, the effort focused upon the case of flow in the tip region of wing with an NACA 0012 airfoil section with a half-rounded tip. The geometric grid was generated using the procedure of Thames (Ref. 33). An example of the grid distribution is shown in Figs. 14 and 15. Figure 14 shows the grid distribution on the surface; Fig. 15 shows the distribution normal to the surface.

The first case considered was for laminar flow at 5° incidence. The Reynolds number based upon chord was 2000, and the calculation was initiated with $\delta/c = .07$. The pressure distribution used was that for

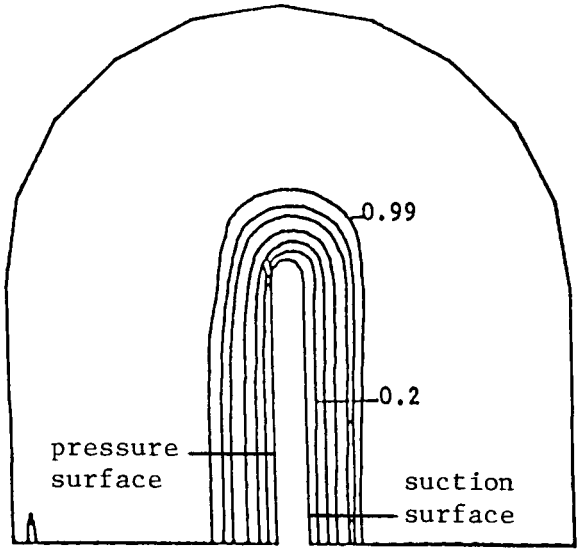

a) x/c = .25

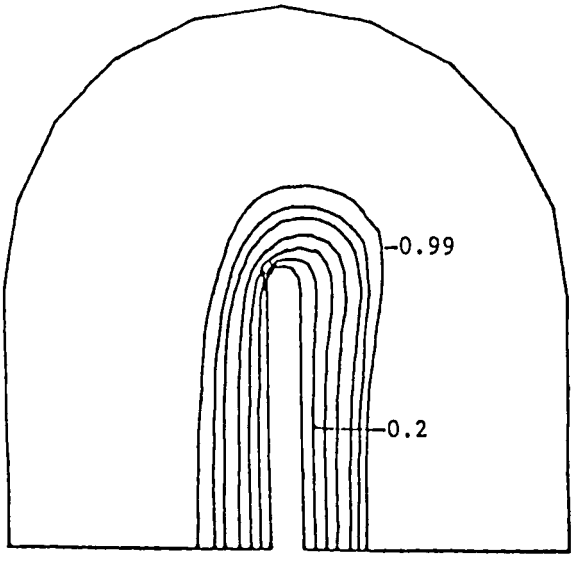

b) x/c = .39

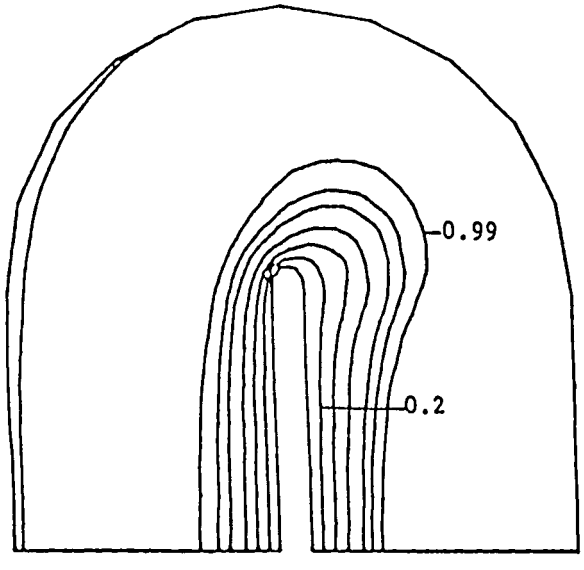

c) x/c = .64

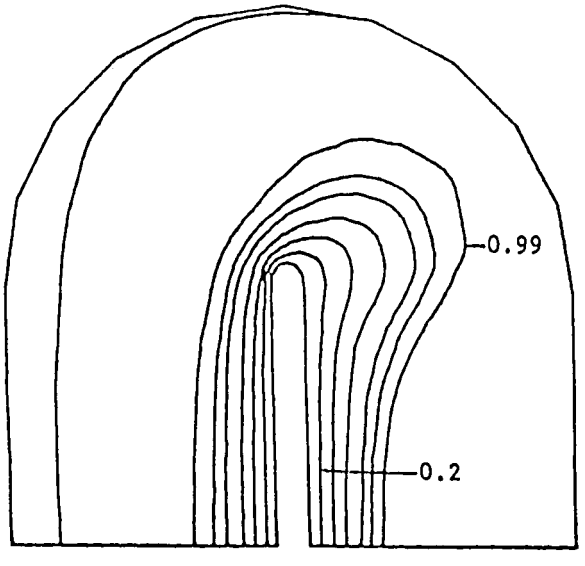

d) x/c = .89

Figure 11. - Contours of streamwise velocity

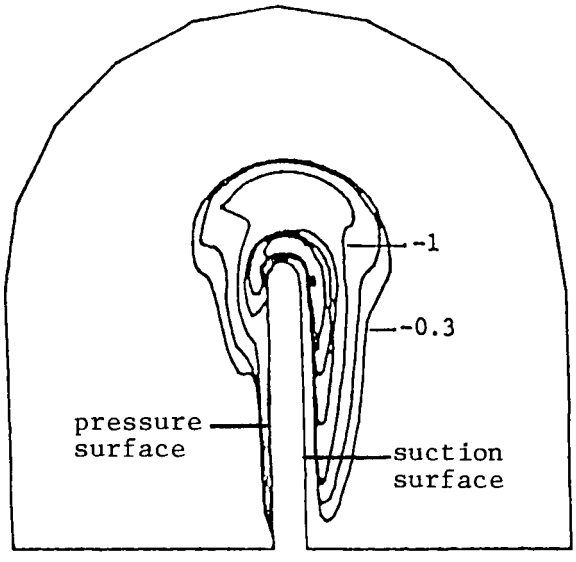

a) x/c = .25

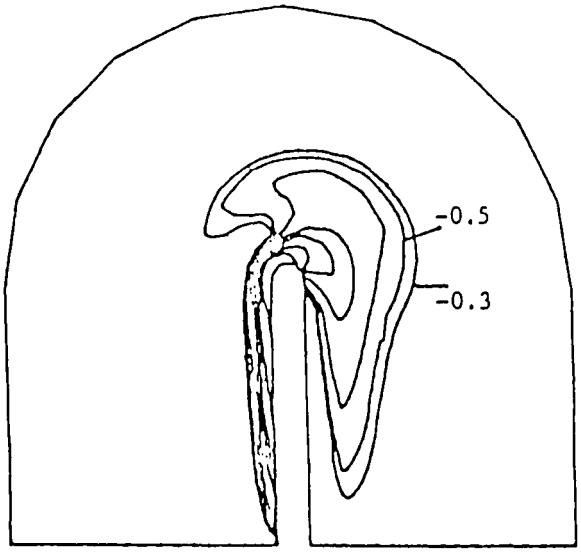

b) x/c = .39

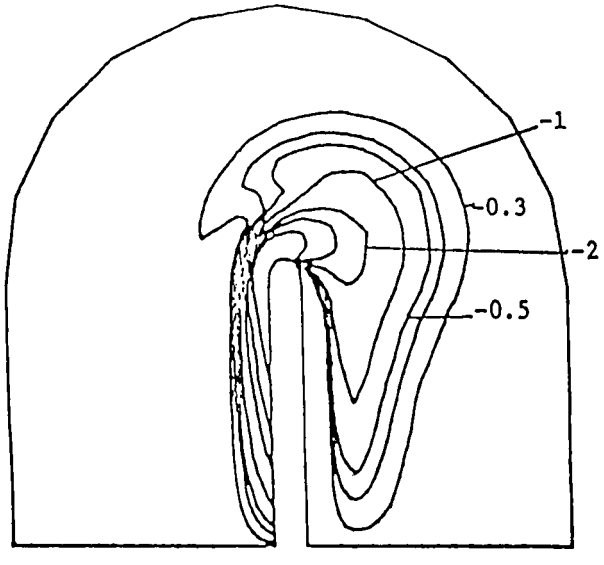

c) x/c = .64

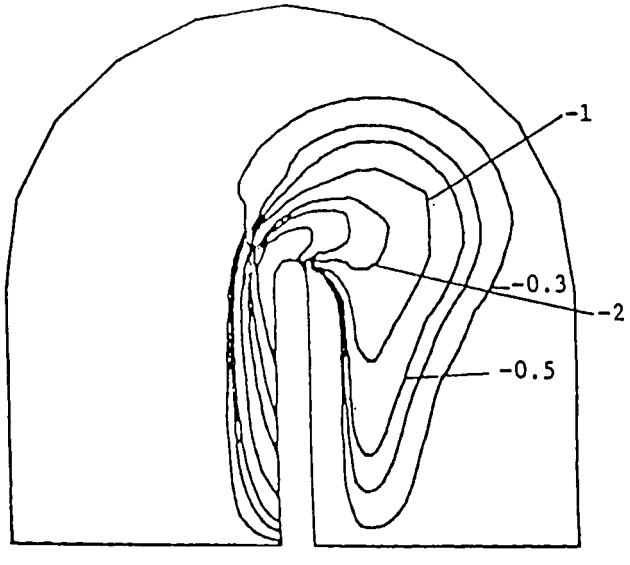

d) x/c = .89

Figure 12. - Contours of streamwise vorticity

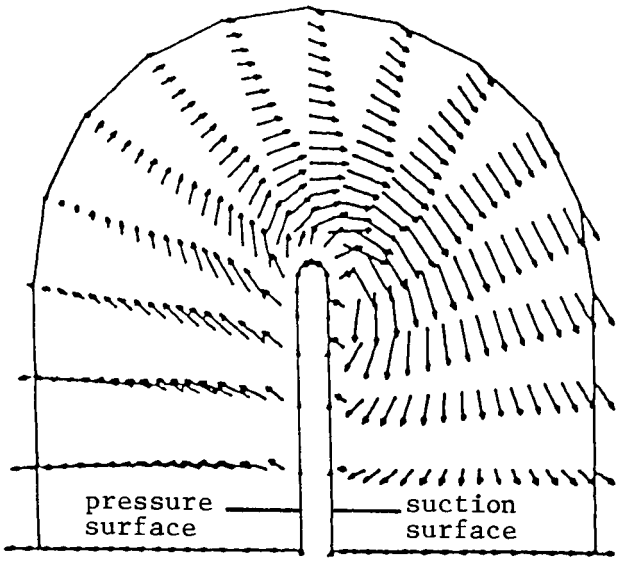

a) x/c = .25

Velocity = 0.07442

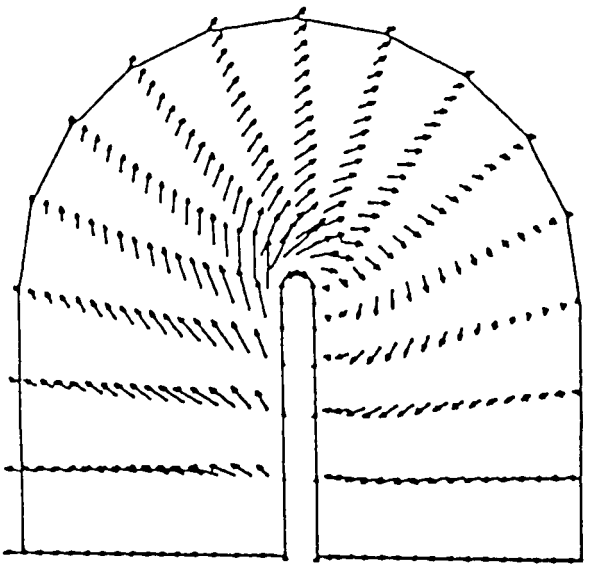

b) x/c = .39

Velocity = 0.14909

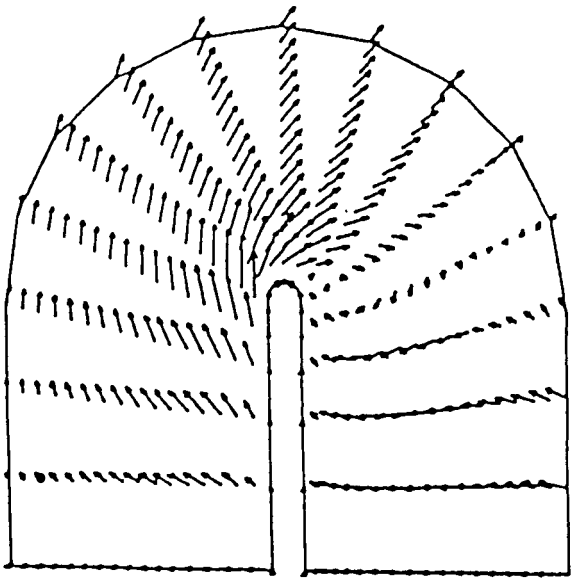

c) x/c = .64

Velocity = 0.15664

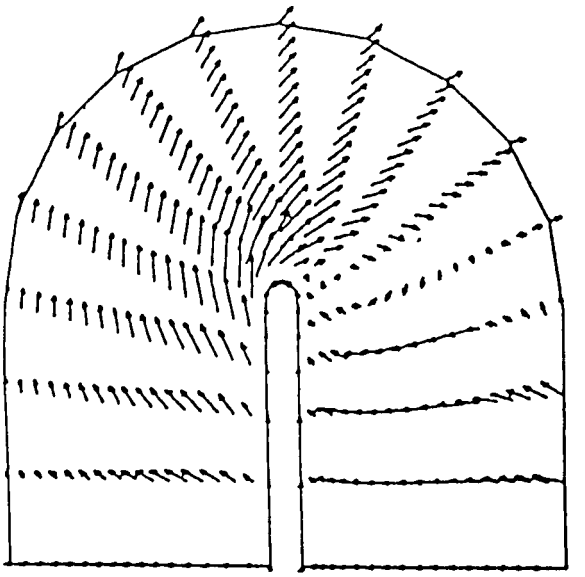

d) x/c = .89

Velocity = 0.16007

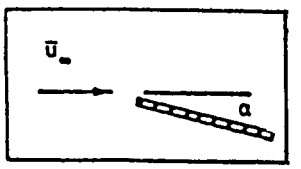

Figure 13. - Secondary flow patterns

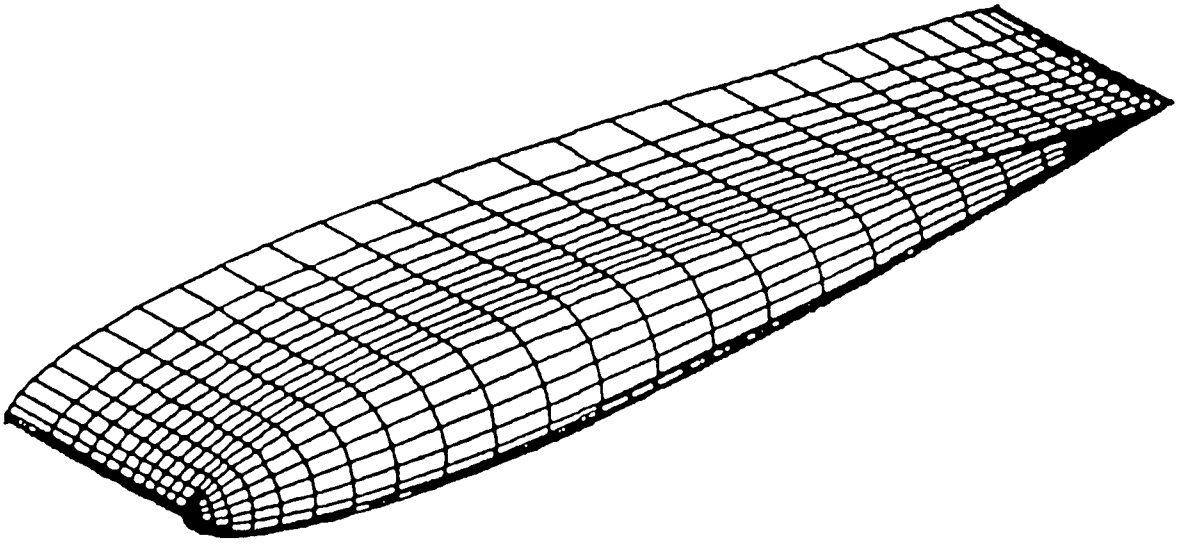

Figure 14. - Grid distribution on surface for wing with NACA 0012 airfoil section

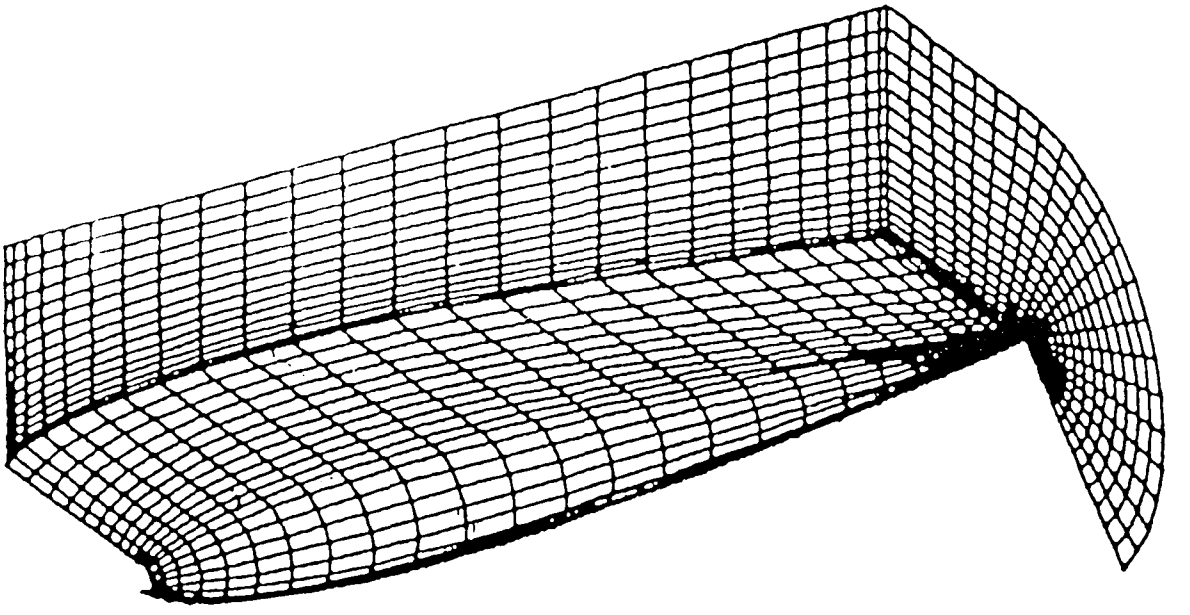

Figure 15. - Three-dimensional plot of grid distribution for wing with NACA 0012 airfoil section

a square tip, and was obtained via the Maskew procedure [Ref. 16]. There are 30 by 33 grid points in the cross section and 20 in the streamwise direction.

It should be noted in the present case that the wing thickness changes with chordline location, and that the wing tip is rounded. Figure 16 presents the contours of streamwise velocity. The streamwise velocity in the tip region is progressively distorted, and shows three-dimensional features as the flow progresses downstream. Figure 17(a) shows the streamwise vorticity at the 19% chord location. At this station, the vorticity is contained within the streamwise boundary layer. The region of high vorticity at the wing tip is the result of the flow from the pressure surface to the suction surface. Further downstream, the vorticity from below the wing tip is convected above the wing and the region of significant streamwise vorticity becomes larger, as shown in Fig. 17. The calculation gave streamwise separation at a location $x/c \approx 0.75$, and was terminated at this location.

The final calculation considered the wing with an NACA 0012 airfoil section in a turbulent flow environment with a Reynolds number based upon a chord of 10^6. The turbulence model used was the simple eddy viscosity model, Eqs. (19) and (20). The grid system at a typical cross-sectional station is given in Fig. 18. The grid is highly stretched so as to resolve the viscous sublayer with the first point being 9×10^{-5} chords from the surface. There are 30 x 33 grid points in cross section and 20 in the streamwise direction. Initial conditions in the present calculation include specification of the streamwise velocity at the first calculation cross plane. The secondary flow velocity is zero initially. Contours of streamwise velocity, streamwise vorticity and secondary flow are presented in Figs. 19-21.

Figures 19-21 show the contours of streamwise velocity, vorticity and secondary flow velocity at stations $x/c = 0.18, 0.3, 0.45, 0.6, 0.71$ from the calculated results. The process of secondary flow development and vortex roll-up seen in the computations again are in general qualitative agreement with experimental results of Chigier and Corsiglia (Ref. 5), Gray, McMahon, Shenoy and Hammer (Ref. 34), and Francis and Kennedy (Ref. 6). As the flow goes downstream, the pressure imbalance between the high pressure below and low pressures above the airfoil drives an irrotational flow in the secondary flow plane from the pressure side outboard, around the tip and finally

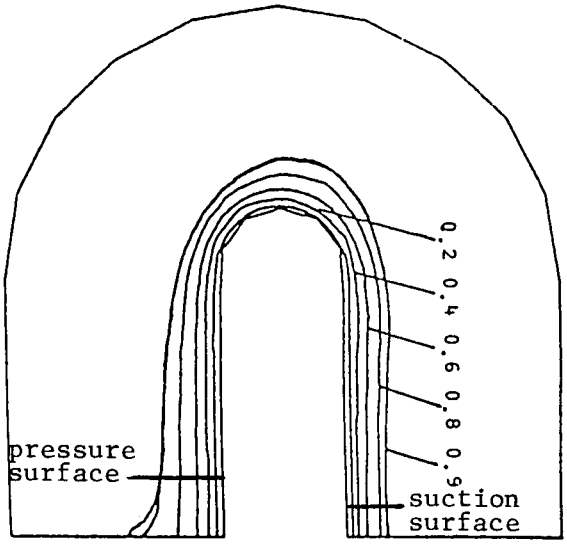

a) x/c = .19

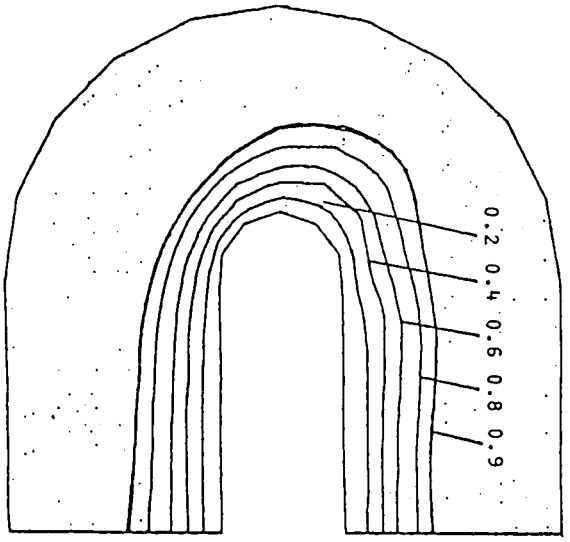

b) x/c = .45

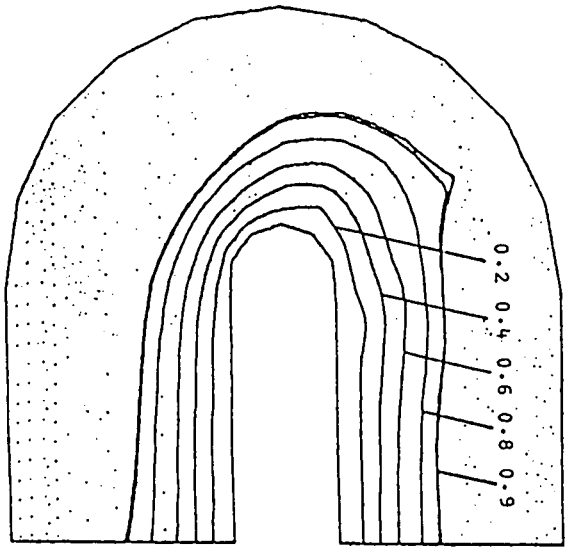

c) x/c = .56

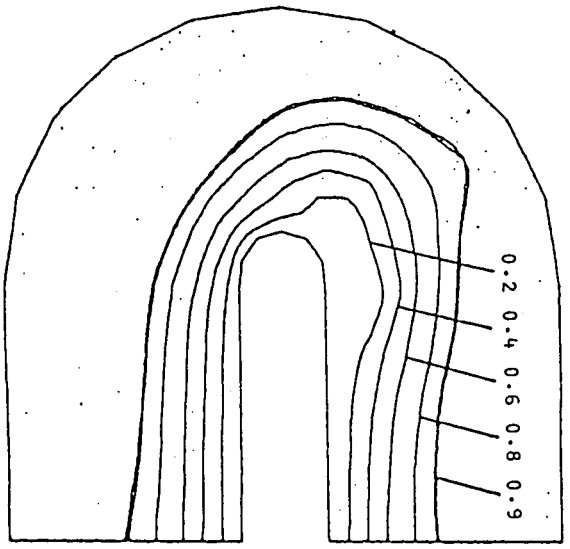

d) x/c = .68

Figure 16. - Contours of streamwise velocity

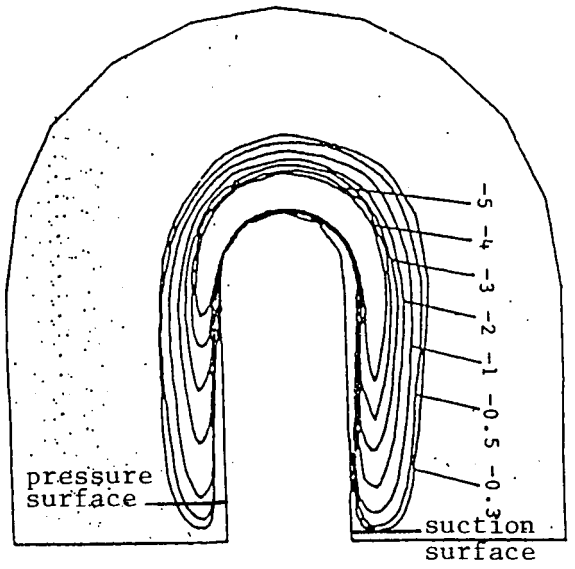

a) x/c = .19

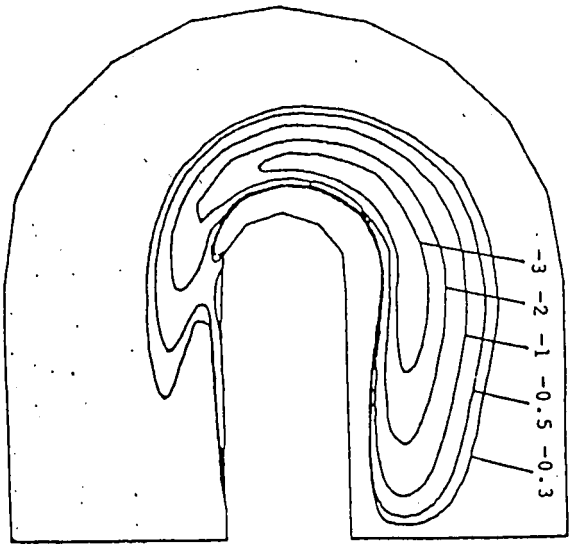

b) x/c = .45

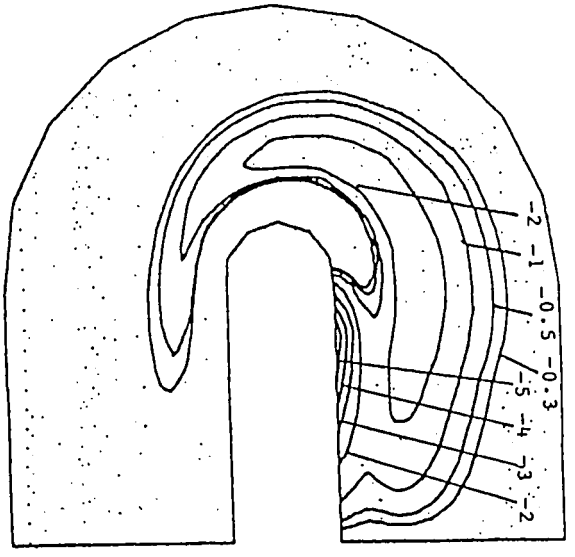

c) = x/c = .56

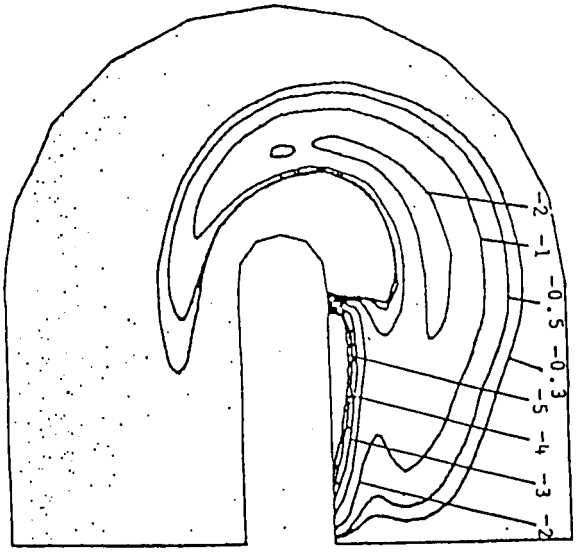

d) x/c = .68

Figure 17. - Contours of streamwise vorticity

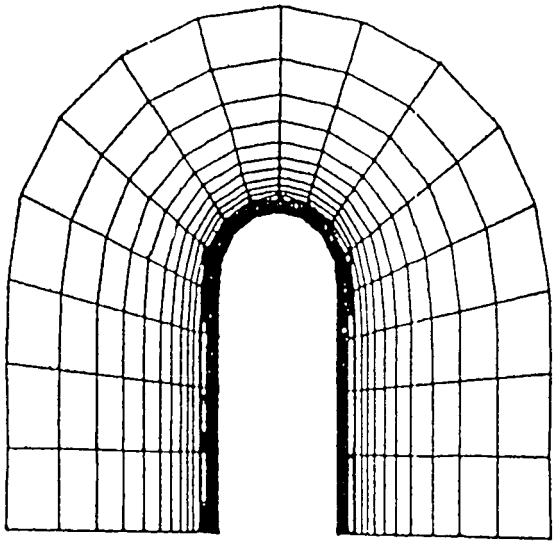

Figure 18. - Grid system in cross section
at station x/c = .18

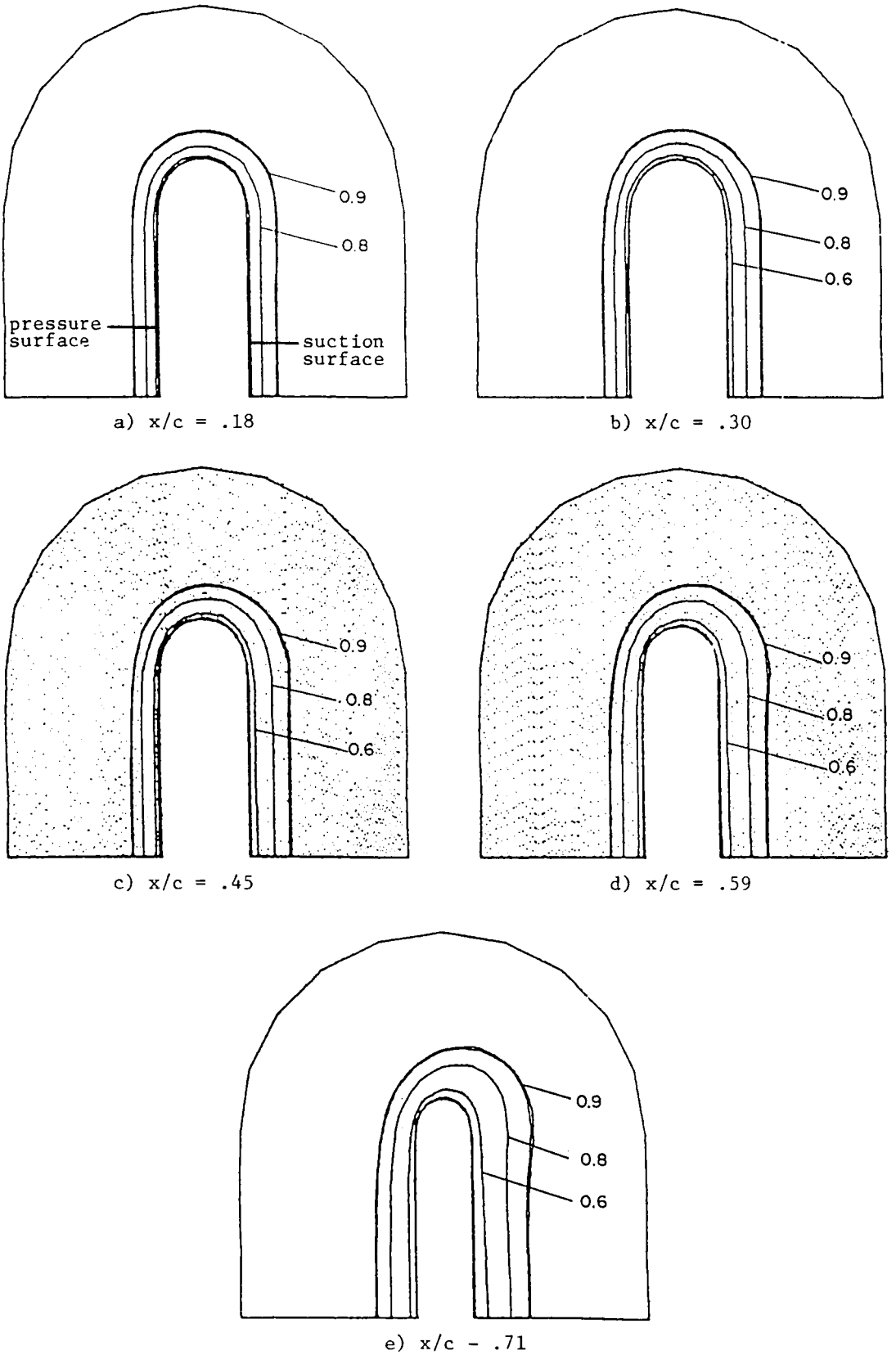

Figure 19. - Contours of streamwise velocity

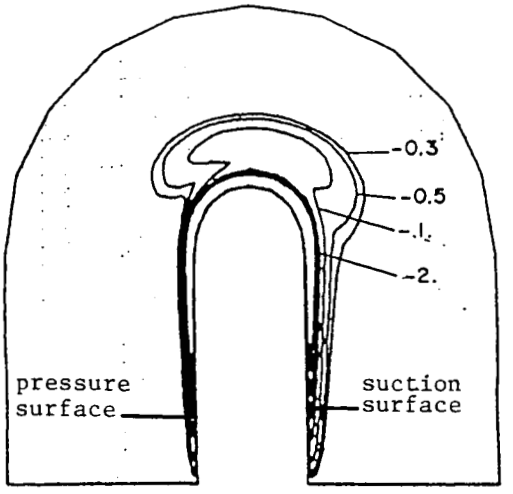

a) x/c = .18

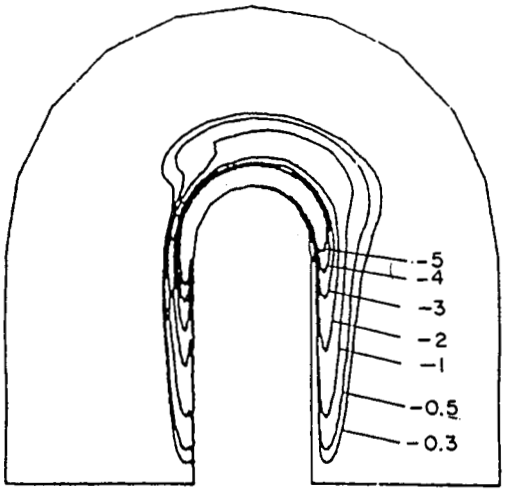

b) x/c = .30

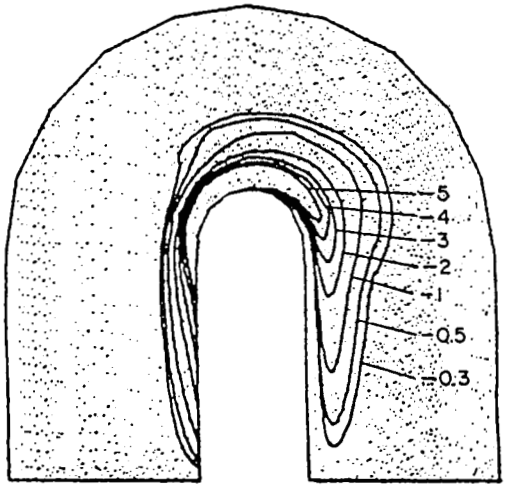

c) x/c = .45

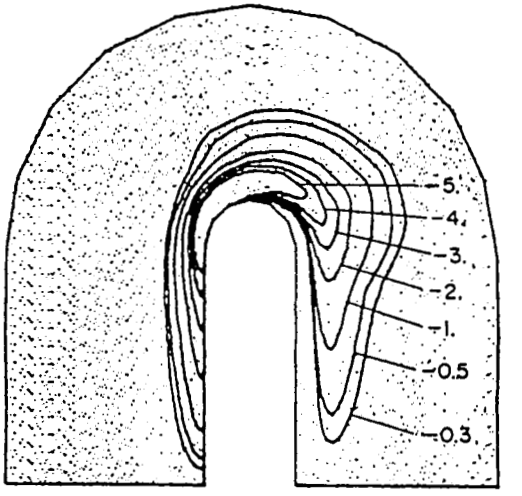

d) x/c = .59

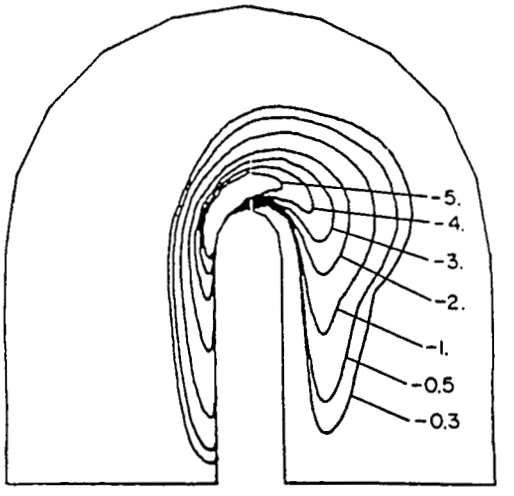

e) x/c = .71

Figure 20. - Contour of streamwise vorticity

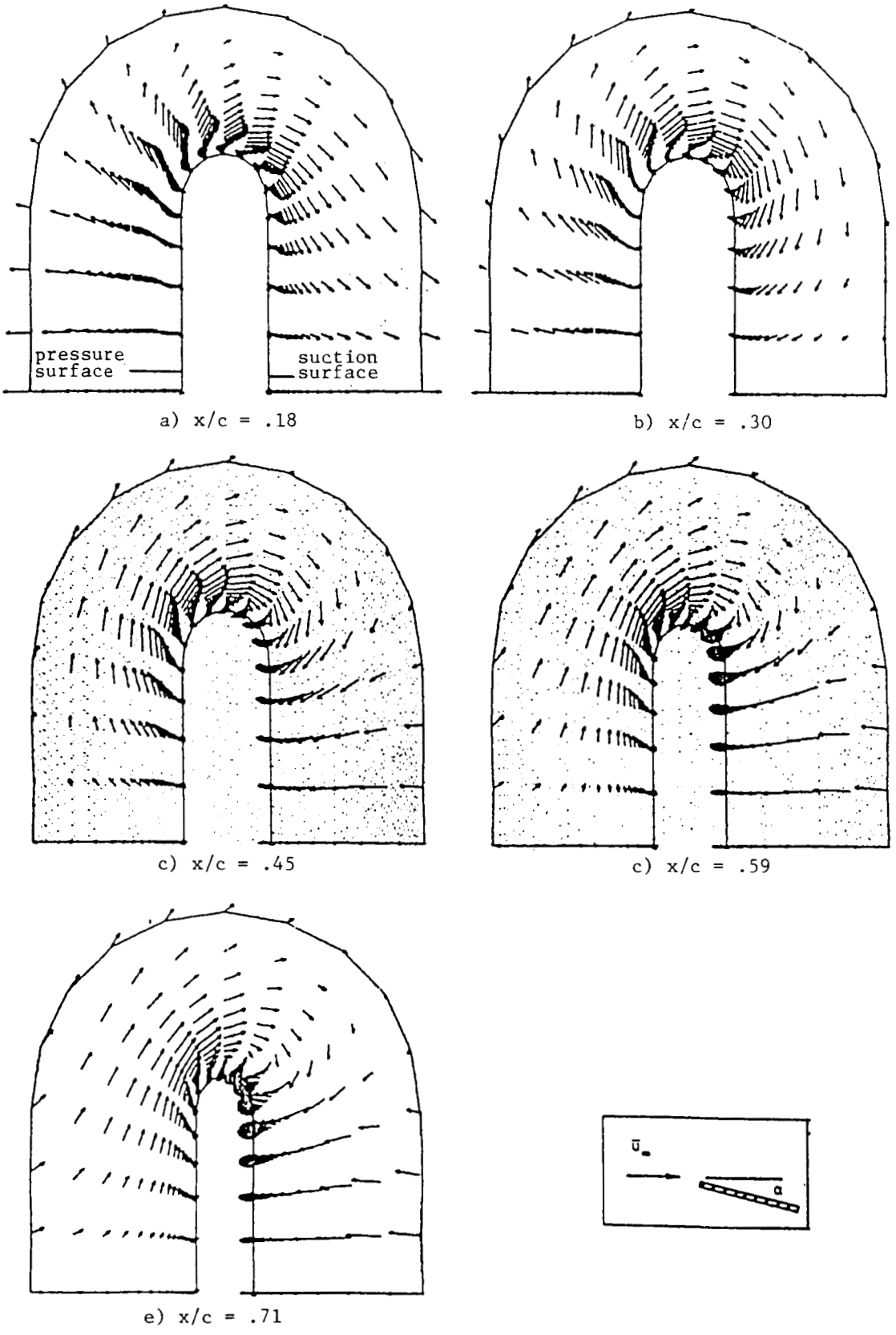

Figure 21. - Secondary flow patterns

inboard on the suction side. This secondary flow pattern is required to obey the no-slip condition at the airfoil surace, and this no-slip condition generates negative vorticity on both the upper and lower surfaces. This physical process is shown clearly in Figs. 20-21.

Contours of streamwise velocity are presented in Fig. 19. In general, these figures show the growth of the streamwise boundary layers. At inboard locations, where the flow is expected to behave two-dimensionally, the streamwise velocity is independent of spanwise coordinate and the pressure surface boundary layers are thinner than the suction surface boundary layer. In the tip region, the flow is strongly three-dimensional due to distortion and skewing of secondary flows as the flow progresses downstream.

As the flow proceeds downstream, the vorticity generated on the pressure surface is convected by the cross flow to the tip, moved around the tip and convected and diffused in a general upward and inboard direction due to continual pressure imbalance. Cross flow separation occurs in the tip region. Above the suction surface a clockwise vortex motion is established which changes the direction of the secondary flow to outward at the wing upper surface. The outward cross flow combined with the no-slip condition results in positive vorticity along the upper surface in the immediate vicinity of the wing. As shown in Fig. 20 the vorticity is beginning to extend outside the streamwise boundary layer at x/c = .30. Figure 20 shows the vorticity contour at stations x/c = 45%, 60%, and 71%. It shows the continuous upward and inboard movement due to continual pressure imbalance between the high pressure below and low pressure above. Also with persistent cross flow separation, the region with positive vorticity in the immediate vicinity of the tip suction surface becomes thicker and larger. This picture of development of the secondary flow pattern is in general agreement of experimental observation by Francis and Kennedy (Ref. 4) and Hoffman and Velkoff (Ref. 35).

Figure 21 shows the vector plot of secondary flow patterns at stations x/c = 18%, 30%, 45%, 59% and 71% with the velocity projected in a plane which is normal to the free streamwise velocity for upstream of the wing rather than the velocity normal to the airfoil. At x/c = 0.18, the cross flow separation has not occurred as the secondary flow pattern simply shows flow around the tip from the pressure surface to the suction surface.
The spanwise velocity is directed outward below the pressure surface and

inward above the suction surface. The vertical velocity is directed upward everywhere. Near the tip region in the pressure surface, there has been small flow reversal driven by the input inviscid pressure field. The inviscid pressure obtained from Maskew (Ref. 16) was only approximate for the present case. The next plot shows the cross flow separation beginning to form at x/c = 0.3. The spanwise velocity is directed outward below the pressure surface and outward near the suction surface and inward far from the suction surface. This result is consistent with the vorticity plot. The next plots show the further development of the secondary flow. As the region of cross flow separation enlarges and thickens, the secondary flow shows a definite circular flow pattern and moves upward. Note that these plots present only a fraction of the grid points used in the flow calculation. In Figs. 21(b)-21(e) the velocity vectors near the suction surface are shown penetrating the wing surface. This represents relatively large normal velocities near the wall. At the wing surface the velocity is zero.

The results shown in Figs. 19-21 clearly show the tip vortex generation process for a NACA 0012 airfoil with rectangular planform and rounded tip. This represents a calculation for an actual geometric configuration of interest at a relevant Reynolds number. In particular, it should be noted that with the rounded tip the center of the vortex appears slightly outboard of the tip in contrast to the square tip where the vortex set up inboard of the tip. This is in agreement with the experimental data of Ref. 34. In regard to quantitative comparisons, the previous comments regarding the square tip still apply and the results appear consistent with those of Chigier and Corsiglia (Ref. 6).

Inboard Boundary Condition Study

The final item considered in the present study focuses upon the sensitivity of the flow to the inboard boundary condition. As previously discussed, the boundary condition along the solid surface satisfied zero streamwise, transverse and spanwise velocity. On the far field boundary streamwise velocity was extrapolated from the interior, scalar potential was set to zero, vector potential was obtained by integrating the component of transverse velocity along the boundary and streamwise vorticity was set to zero. In the calculations done previously, the spanwise velocity was set to

zero at the inboard boundaries and the spanwise velocity derivative was set to zero.

Under this portion of the effort the inboard boundary conditions were reconsidered. They represent the influence of the inboard sections on the wing tip flow field. Thus, the specifications of the inboard boundary conditions should be related to the velocity field of the wing which contains the influence of the lift distribution and the trailing vortex sheet of the entire wing. With these considerations in mind, a revised inboard boundary condition was formulated. In this approach a spanwise velocity distribution along the inboard boundaries compatible with the viscous flow equations is obtained from solution of the coupled vector potential-vorticity equations along the inboard boundaries utilizing the inviscid spanwise velocity as an outer boundary condition. Neglecting spanwise variations, the coupled vector potential-vorticity equations are solved as a two-point boundary value problem along the inboard boundaries. Boundary conditions are specified from the no-slip and no through-flow velocity conditions on the wing surface (at B - C of Fig. 22), and the inviscid spanwise velocity and zero streamwise vorticity at the outer boundary (at A - D). The solution to the vector potential is used as the inboard boundary condition for the coupled vector potential-vorticity equations for the interior tip flow field. When an inviscid velocity field about the wing is available, the spanwise velocity boundary condition is derived from this flow field as outlined in the following paragraphs. If an inviscid flow field is not available, the required inviscid flow information can be approximated from the induced velocity field derived from an assumed spanwise lift distribution as will also be discussed shortly.

For the purposes of a computation demonstrating application of this new boundary condition formulation, the tip flow field for a slab wing with a rounded tip at a geometric angle of attack of 6° were computed. The flow was laminar with a Reynolds number of 1000.0 based on the thickness (t) of the wing section or 20,000 based on chord.

The inviscid transverse velocities were assumed to be composed of the potential flow due to the geometric angle of attack and the induced velocity field due to the trailing vortex sheet. The induced velocities were computed from the simple Prandtl lifting line theory of finite wings. The inviscid spanwise velocities at the inboard boundaries for the two point boundary

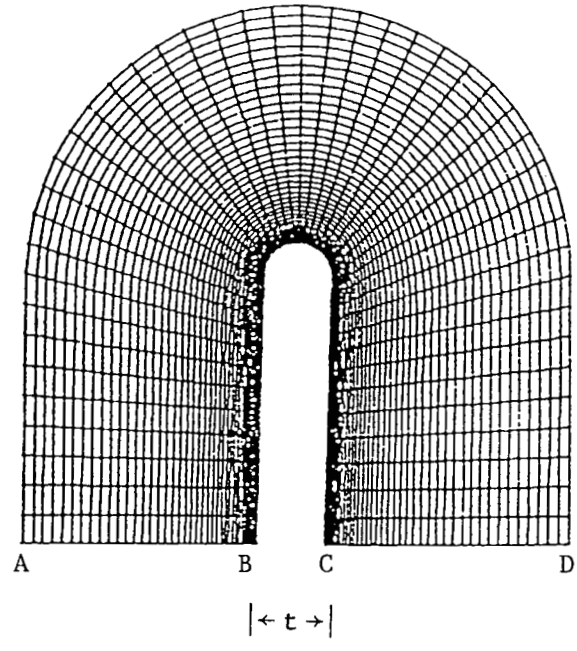

Figure 22. - Computational domain and grid at a typical streamwise station

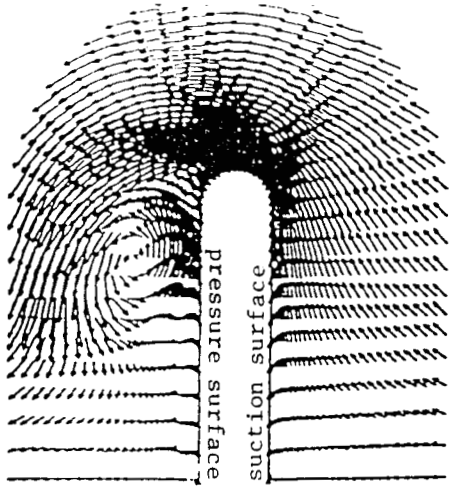

a) no induced velocities

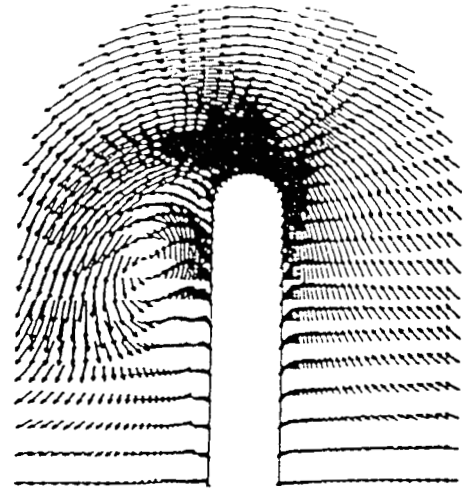

b) aspect ratio = 20.0

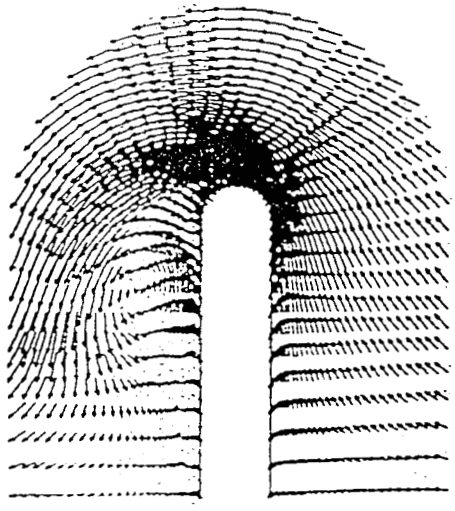

c) aspect ratio = 10.0

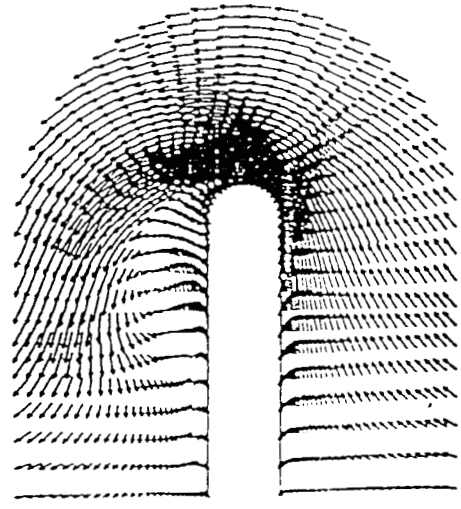

d) aspect ratio = 7.5

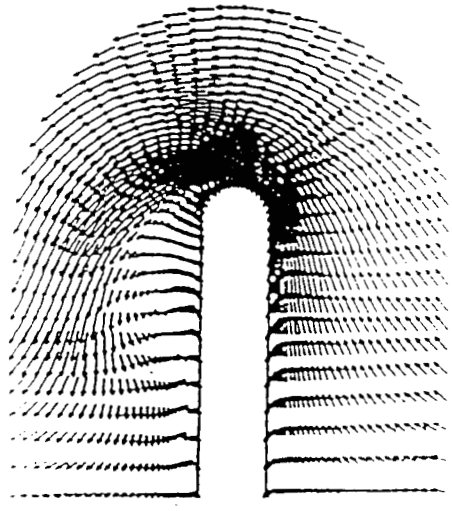

e) aspect ratio = 5.0

Figure 23. - Effect of wing aspect ratio on transverse velocity fields at x/t = 20.0

value problem were also computed from the trailing vortex sheet. A linear lift distribution was assumed on the wing resulting in a trailing vortex sheet of constant strength.

Figure 23 shows a vector plot of the transverse velocity field at $x/t = 20.0$. The induced velocities in this first calculation were set to zero assuming no flow penetration of the inboard boundaries. The strong tip vortex is evident. Figure 23 also shows the computed transverse velocity field at $x/t = 20.0$ with the induced velocities computed for wings with aspect ratio 20.0, 10.0, 7.5, and 5.0, respectively. The strength of the tip vortex decreases corresponding to larger induced velocities from the trailing vortex sheet. It should be noted that induced velocity increases as the aspect ratio decreases. The spanwise velocities at the inboard boundaries are small in all the cases, being largest at the aspect ratio of 5. The dominant effect of the induced velocities on the tip vortex is from the normal component of the induced velocity which reduces the effective angle of attack on the wing. General conclusions about the effect of aspect ratio on the tip vortex cannot be drawn from these demonstration computations due to the approximations in the computation of the induced velocity field and the difference in lift of the wings. However, the computations do demonstrate a newly developed method of specifying boundary conditions on the inboard boundaries that relate the tip flow field with the overall inviscid flow on the wing.

CONCLUDING REMARKS

The present effort has developed a three-dimensional viscous flow forward marching analysis for the tip vortex generation problem. In contrast to other more approximate analyses which model the process with inviscid equations, and rely upon a semi-empirical model to determine the shed vorticity, the present procedure calculates shed vorticity from the basic cross-flow separation mechanism and the subsequent convection of this vorticity downstream. The analysis is based upon solution of a streamwise momentum equation, a streamwise vorticity equation, a secondary flow stream function equation and the continuity equation. High near wall resolution is obtained in the process and no-slip conditions for all components of velocity are enforced at the airfoil surface. In its present form, the analysis requires an estimate of the inviscid streamwise pressure gradient which must be obtained from an external source such as a vortex lattice method or a panel method with lift.

The procedure has been applied to a constant thickness slab wing with a square tip, a constant thickness slab wing with a half round tip and a NACA 0012 wing with a rounded tip. In the latter case, the coordinate system used was a body fitted nonorthogonal system developed by Thames. The analysis has been applied to both laminar flow and turbulent flow with a simple eddy viscosity model being used to represent the turbulent shear. The turbulent high Reynolds number calculation required a highly stretched grid to obtain the required wall resolution.

The effort has concentrated upon two items: (i) the tip vortex generation process and (ii) quantitative results. As far as the generation process is concerned, the basic mechanism shown in the calculations is in good agreement with experimental data. When a wing is immersed in a flow at non-zero incidence, a pressure differential develops between the upper and lower surfaces. As the tip is approached, this differential decreases since outboard of the tip no pressure discontinuity can exist. The pressure imbalance causes flow outward on the pressure surface, upward at the tip and inward on the suction surface. This secondary flow must obey the wall no-slip condition thus generating streamwise vorticity in the form of a cross flow boundary layer which is convected from the pressure surface to the tip where it separates and forms the tip vortex. The present predictions of

vortex appearance, path, strength and secondary flow field are reasonable when compared with existing experimental data. However, detailed comparisons with high quality experimental measurements are needed to validate the quantitative flow predictions of the analysis.

REFERENCES

1. Scheiman, J., Megrail, J.L. and Shivers, J.P.: Exploratory Investigation of Factors Affecting the Wing Tip Vortex, NASA TM X-2516, 1972.

2. Thompson, D.H.: An Experimental Study of Axial Flow in Wing Tip Vortices, Australian Defense Scientific Service Aeronautical Research Laboratories Report ARL/A 355, 1975.

3. Spivey, W.A. and Morehouse, G.G.: New Insights into the Design of Swept Tip Rotor Blades, American Helicopter Society Preprint 420, 1970.

4. Francis, M.S. and Kennedy, D.A.: Formation of a Trailing Vortex, Journal of Aircraft, Vol. 16, 1979.

5. Chigier, N.A. and Corsiglia, V.R.: Tip Vortices - Velocity Distributions, American Helicopter Society Preprint No. 552, 1971.

6. Chigier, N.A. and Corsiglia, V.R.: Tip Vortices - Velocity Distributions, 27th Annual National V/STOL Forum, AHS, Washington, DC, 1971.

7. Geissler, W.: Dynamic Stall Investigations on a Rectangular Blade Tip, DFVLR Report IB 232-82 J04, 1982.

8. Shivananda, T.P., McMahon, H.M. and Gray, R.B.: Surface Pressure Measurements at the Tip of a Model Helicopter Rotor in Hover, Journal of Aircraft, Vol. 15, 1978, pp. 460-467.

9. Platzer, G.P. and Souders, W.G.: Tip Vortex Cavitation Delay with Application to Marine Lifting Surfaces - A Literature Search, David Taylor Naval Ship Research and Development Center, Rpt. 79/051, August 1979.

10. Souders, W.G. and Platzer, G.P.: Tip Vortex Cavitation Characteristics and Delay of Inception on a Three-Dimensional Hydrofoil, David Taylor Naval Ship Research and Development Center, Rpt. 81/007, April 1981.

11. Jessup, S.D.: Measurements of Pressure Distribution on Two Model Propellers, David Taylor Naval Ship Research and Development Center, Rpt. 82/035, July 1982.

12. Iversen, J.D.: Correlation of Turbulent Trailing Vortex Decay Data, Journal of Aircraft, Vol. 13, May 1976, pp. 338-342.

13. Kandil, O.A., Mook, D.T. and Nayfeh, A.H.: Nonlinear Prediction of Aerodynamic Loads on Lifting Surfaces, Journal of Aircraft, Vol. 13, January 1976, pp. 22-28.

14. Kandil, O.A., Mook, D.T. and Nayfeh, A.H.: Subsonic Loads on Wings having Sharp Leading Edges and Tips, Journal of Aircraft, Vol. 13, January 1976, pp. 62-63.

REFERENCES (Continued)

15. Rehbach, C.: Numerical Investigation of Leading Edge Vortex for Low Aspect Ratio Thin Wings, Journal of Aircraft, Vol. 13, February 1976, pp. 253-255.

16. Maskew, B.: Prediction of Subsonic Aerodynamic Characteristics: A Case for Low Order Panel Methods, Journal of Aircraft, Vol. 19, No. 2, 1982.

17. Kerwin, J.E. and Lee, C.S.: Prediction of Steady and Unsteady Propeller Performance by Numerical Lifting-Surface Theory, Society of Naval Architects and Marine Engineers Transactions, Vol. 86, 1978.

18. Greeley, D.S. and Kerwin, J.E.: Numerical Methods for Propeller Design and Analysis in Steady Flow, Transactions, Society of Naval Architectures and Marine Engineers, Vol. 90, 1982.

19. Brockett, T.: Propeller Perturbation Problems, David Taylor Naval Ship Research and Development Center, Rpt. 3880, 1972.

20. Shamroth, S.J.: Calculation of Steady and Oscillating Airfoil Flow Fields via the Navier-Stokes Equations, AIAA Paper 84-525, 1984.

21. Briley, W.R. and McDonald, H.: Computation of Three-Dimensional Horseshoe Vortex Flow Using the Navier-Stokes Equations. Paper presented at 7th International Conference on Numerical Methods in Fluid Dynamics, 1980.

22. Briley, W.R. and McDonald, H.: Analysis and Computation of Viscous Subsonic Primary and Secondary Flows, AIAA Paper No. 79-1453, 4th Computational Fluid Dynamics Conference, Williamsburg, VA, 1979.

23. Briley, W.R. and McDonald, H.: Three-Dimensional Flows with large Secondary Velocity, SRA Rpt. R83-900007-F, July 1983. (Also Journal of Fluid Mechanics, Vol. 144, pp. 47-77, 1984).

24. Levy, R., Briley, W.R. and McDonald, H.: Viscous Primary/Secondary Flow Analysis for Use with Nonorthogonal Coordinate Systems, AIAA Paper 83-0556, 1983.

25. Kreskovsky, J.P., Briley, W.R. and McDonald, H.: Investigation of Mixing in a Turbofan Exhaust Duct, Part I: Analysis and Computational Procedure, AIAA Journal, March 1984.

26. Kreskovsky, J.P., Briley, W.R. and McDonald, H.: Analysis and Computation of Three-Dimensional Flow in Strongly Curved Ducts, Computers in Flow Predictions and Fluid Dynamics Experiments, ASME Winter Annual Meeting, 1981.

27. Shamroth, S.J. and Briley, W.R.: A Viscous Flow Analysis of the Tip Vortex Generation Process, AIAA Paper 79-1546, 1979. (Also NASA CR-3184).

REFERENCES (Continued)

28. Govindan, T.R., Levy, R. and Shamroth, S.J.: Computation of The Ship Vortex Generation Process for Ship Propeller Blades, SRA Rpt. R83-920021-F. Final report presentd under Contract N00014-83-C-0768 for the Office of Naval Research, 1984.

29. Kreskovsky, J.P., Briley, W.R. and McDonald, H.: Prediction of Laminar and Turbulent Primary and Secondary Flows in Strongly Curved Ducts, NASA CR-3388, February 1981.

30. Briley, W.R. and McDonald, H.: On the Structure and Use of Linearized Block Implicit Schemes, Journal of Computational Physics, Vol. 34, 1980.

31. Roberts, G.O.: Computational Methods for Boundary Layer Problems, Proceedings of the Second International Conference on Numerical Methods in Fluid Dynamics, Springer-Verlag, New York, 1971.

32. Clauser, F.H.: Turbulent Boundary Layers in Adverse Pressure Gradients, Journal of the Aeronautical Sciences, Vol. 21, 1954, pp. 91-108.

33. Thames, F.C.: Generation of Three-Dimensional Boundary Fitted Curvilinear Coordinate Systems For Wing/Wing Tip Geometries Using the Elliptic Solver Method, Symposium on Numerical Generation of Curvilinear Coordinate Systems, Nashville, 1982.

34. Gray, R.B., McMahon, H.M., Shenoy, K.R. and Hammer, M.L.: Surface Pressure Measurements at Two Tips of a Model Helicopter Rotor in Hover, NASA CR-3281, 1980.

35. Hoffman, J.D. and Velkoff, H.R.: Vortex Flow over Helicopter Rotor Tips, Journal of Aircraft, Vol. 8, No. 9, September 1971, pp. 739-740.

1. Report No.	2. Government Accession No.	3. Recipient's Catalog No.
NASA CR-3906		

4. Title and Subtitle	5. Report Date
A Three-Dimensional Viscous Flow Analysis for the Helicopter Tip Vortex Generation Problem	August 1985
	6. Performing Organization Code
7. Author(s)	8. Performing Organization Report No.
S-J. Lin, R. Levy, S.J. Shamroth, T.R. Govindan	
	10. Work Unit No.
9. Performing Organization Name and Address	11. Contract or Grant No.
Scientific Research Associates, Inc. P.O. Box 498 Glastonbury, CT 06033	NAS1-14904
	13. Type of Report and Period Covered
12. Sponsoring Agency Name and Address	Contractor Report
National Aeronautics and Space Administration Washington, DC 20546	14. Sponsoring Agency Code

15. Supplementary Notes

Langley Project Manager: James T. Howlett
Final Report

16. Abstract

The tip vortex flow field occurring in the vicinity of the tip region of a a helicopter rotor blade is a very complicated three-dimensional, viscous flow phenomenon. The details of the flow in the tip region can have a major effect in determining the generated rotor noise and can significantly affect the performance and dynamic loading of the rotor blade. In the present study, the three-dimensional viscous subsonic tip vortex generation processes is investigated by a numerical procedure which allows spatial forward-marching integration, utilizing flow approximations from the velocity-decomposition approach of Briley and McDonald. The approach has been applied to compute the laminar and turbulent tip vortex flows for a constant thickness slab airfoil with a square tip, a constant thickness slab airfoil with a half round tip and a NACA 0012 airfoil with a half round tip. The basic mechanism of the tip vortex generation process as well as the prediction of vortex appearance, strength and secondary flow shown by the calculations are in qualitative agreement with experimental results.

17. Key Words (Suggested by Author(s))	18. Distribution Statement
Tip Vortex, Helicopter Spatial Marching Procedure Navier-Stokes Equations	Unclassified - Unlimited Subject Category 02

19. Security Classif. (of this report)	20. Security Classif. (of this page)	21. No. of Pages	22. Price
Unclassified	Unclassified	68	A04

For sale by the National Technical Information Service, Springfield, Virginia 22161

NASA-Langley, 1985